Linear Regression Analysis of 2D Projection Image Data of 6 Degrees-of-Freedom Transformed 3D Image Sets for Stereotactic Radiation Therapy

by
Christie Lin

Submitted to the Department of Nuclear Science and Engineering
in partial fulfillment of the requirements for the degrees of

Bachelor's of Science Degree in Nuclear Science and Engineering
and
Master's of Science Degree in Nuclear Science and Engineering

at the
MASSACHUSETTS INSTITUTE OF TECHNOLOGY

June 2012

Author.....
Christie Lin
Department of Nuclear Science and Engineering, Massachusetts Institute of Technology
May 11, 2012

Certified by.....
Richard C. Lanza
Senior Research Scientist, Massachusetts Institute of Technology
Thesis Supervisor

Certified by.....
Brian Winey
Physicist, Massachusetts General Hospital
Thesis Supervisor

Certified by.....
Paola Cappellaro
Assistant Professor of Nuclear Science and Engineering
Thesis Reader

Accepted by.....
Mujid S. Kazimi
TEPCO Professor of Nuclear Engineering
Chair, Department Committee on Graduate Students

Linear Regression Analysis of 2D Projection Image Data of 6 Degrees-of-Freedom Transformed 3D Image Sets for Stereotactic Radiation Therapy

By

Christie Lin

Submitted to the Department of Nuclear Science and Engineering
on May 11, 2012, in partial fulfillment
of the requirements for the degrees of
Bachelor's of Science Degree in Nuclear Science and Engineering
and
Master's of Science Degree in Nuclear Science and Engineering

ABSTRACT

Patient positioning is crucial to accurate dose delivery during radiation therapy to ensure the proper localization of dose to the target tumor volume. In patient positioning for stereotactic radiation therapy treatment, classical image registration methods are computationally costly and imprecise. We developed an automatic, fast, and robust 2D-3D registration method to improve accuracy and speed of identifying 6 degrees-of-freedom (DoF) transformations during patient positioning for stereotactic radiotherapy by creating a model of characteristic shape distributions to determine the linear relationship between two real-time orthogonal 2D projection images and the 3D volume image. We defined a preprocessed sparse base set of shape distributions that characterize 2D digitally reconstructed radiograph (DRR) images from a range of independent transformations of the volume. The algorithm calculates the 6-DoF transformation of the patient based upon two orthogonal real-time 2D images by correlating the images against the base set. The algorithm has positioning accuracy to at least 1 pixel, equivalent to 0.5098 mm accuracy given this image resolution. The shape distribution of each 2D image is created in MATLAB in an average of 0.017 s. The online algorithm allows for rapid and accurate position matching of the images, providing the transformation needed to align the patient on average in 0.5276 s. The shape distribution algorithm affords speed, robustness, and accuracy of patient positioning during stereotactic radiotherapy treatment for small-order 6-DoF transformations as compared with existing techniques for the quantification of patient setup where both linear and rotational deviations occur. This algorithm also indicates the potential for rapid, high precision patient positioning from the interpolation and extrapolation of the linear relationships based upon shape distributions.

Key words: shape distribution, image registration, patient positioning, radiation therapy

Thesis Supervisor: Brian Winey
Title: Physicist, Massachusetts General Hospital
Thesis Supervisor: Richard C. Lanza
Title: Senior Research Scientist, Massachusetts Institute of Technology

Acknowledgements

First, I would like to thank my two thesis advisors, Dr. Brian Winey and Dr. Richard Lanza. Thank you for the encouragement and support throughout this entire project. Their patience and excitement were truly appreciated. Dr. Brian Winey was instrumental in introducing me to the medical physics community by bringing me into radiation therapy treatments, enrolling me in supportive courses, and providing me with resources and time whenever they were needed. Thanks for answering my questions and believing in my ideas!

A big thanks goes to the Department of Nuclear Science and Engineering at the Massachusetts Institute of Technology and the Department of Radiation Oncology at Massachusetts General Hospital for support in this collaborative project. I was very fortunate to be able to engage with the wonderful people in both of these intellectual communities.

Last but not least, I would like to express my appreciation for the constant encouragement and love from my family and friends. Thanks to my mom, dad, and sister for sending love from miles away. I could not have found this project without Matthew Davidson; thank you for helping me find resources to support my many research interests over the last few years. Thanks to my roommates and hermit crabs for making Hippo a happy home. To the mathematicians and computer scientists, it has been a pleasure to discuss this project with you! Extreme gratitude goes out to Bryan Haddon for helping along every step of this process from listening to my ideas to developing figures in the final push. I would not be here today without the support from all of these people who gave me the strength and determination to complete this work. All in all, what I have really learned is that I am addicted to learning!

This project is supported by the National Cancer Institute Federal Share of program income earned by Massachusetts General Hospital on C06 CA059267, Proton Therapy Research and Treatment Center.

A final note: any mistakes in this document are solely my own and in no way are a reflection of the people who supported this thesis.

Contents

List of Figures

List of Tables

1. Introduction

Cancer is a classification of diseases due to the uncontrolled growth of cells. The National Cancer Institute estimates that in the United States in 2012 alone, there will be 1,638,910 new cases of, and 577,190 deaths due to cancer [1].[a] Cancer is a leading cause of death, accounting for about 13% of all deaths worldwide in 2008 [1]. While the overall rate of new cancer cases has significantly declined [2], deaths from cancer worldwide are projected to continue rising, with an estimated 13.1 million deaths in 2030 [3]. Cancer treatment requires a careful selection of one or more interventions, such as surgery, radiation therapy, and chemotherapy [4].

One of the greatest advances in research and technology of cancer treatments has been the utilization of ionizing radiation. Ionizing radiation damages the DNA of tumor cells, which kills the cells or limits their proliferation. The first step in using ionizing radiation for cancer treatment is for the clinical team to plan the radiation treatment specific for each patient for the dose to conform to the tumor. One important element in effectively delivering the ionizing radiation to the cancer patient is the accurate alignment of the patient in the treatment room with respect to the conformal radiation beam. A major source of concern in radiation therapy is the improper knowledge of the patient's anatomy and suboptimal patient positioning during the course of therapy, which can drastically compromise the clinical results. Reduction of these uncertainty margins can be achieved with accurate patient positioning before treatment.

Among the weakest links in the treatment planning process is the problem of patient positioning and immobilization [5]. Current image registration processes are lengthy and have significant margins of error. In fact, this problem of alignment remains the area of greatest variance in actual treatment [5]. Medical imaging by computed tomography and digitally reconstructed radiographs provides an anatomical representation of the patient and can be interpreted to align the patient in the treatment rooms. This thesis addresses the need for a faster and more accurate patient positioning algorithm that would be easy to deploy, reduces radiation imparted to the patient, improves radiation dose delivery with speed and precision, and facilitates more efficient use of radiation treatment rooms.

1.1 Radiation Therapy

Radiation therapy, or radiotherapy, is the use of ionizing radiation to treat tumors and kill cancer cells. Radiation therapy can be given with a curative intent to cure cancer by eliminating the tumor or preventing cancer recurrence, or with a palliative intent to relieve symptoms and reduce cancer-induced suffering [6]. As a curative intent, radiation therapy is used for approximately half of all cancer cases and often in conjunction with chemotherapy and surgery [7,8]. Advances in radiation therapy have led to increased survival and improved quality of life for patients with the improvement of radiation dose conforming to the tumor and minimizing dose delivered to healthy tissue [9]. With advances in techniques to measure and deliver dose effects, the effectiveness of radiation therapy on tumor treatment has been improving.

---

[a] not including non-melanoma skin cancers

1.1.1 History of Radiation Therapy

Radiation therapy is a relatively new idea that was born just over 100 years ago with the discovery of radioactive isotopes. This discovery prompted scientists to investigate the effects of radiation on the body with the particular interest to use it advantageously for health benefits or cure.

With the discovery of x-rays by Wilhelm Conrad Roentgen in 1895, and the discovery of radium by Marie Curie in 1898, scientists saw the effects of x-rays and radium on hair loss and skin damage [10]. Soon after, physicians found x-rays useful for diagnosing broken bones and locating foreign objects, like bullets, in the body. The therapeutic benefits of radium were first commercially exploited in 1913 for treating breast cancer, head cancer, cervical cancer, and lymph nodes. However, radiation therapy treatments for ailments were largely reserved for only inoperable, unresectable, or recurrent tumors because of inexperience in radiation treatment planning.

In the mid-1900s, physicists and biologists conducted extensive research on how radiation works, how to measure radiation dose, and how to control radiation. Increase in funding in these studies on radiation was supported by the Americans, as the American media bloomed with articles and reports calling for great need for action against cancer, and soon the National Cancer Institute was born [10]. After World War II, cyclotrons and nuclear reactors were available to accelerate particles to very high energies and produce synthetic radioactive isotopes. In 1953, Henry Kaplan created the medical linear accelerator x-ray machine. These three new devices were key in improving cancer cure rates and the applicability of radiation therapy expanded to also include Hodgkin's lymphomas and testicular cancers.

Radiation treatment therapy became a more viable treatment option for cancers in the 1970s with the introduction of computers to assist in treatment planning. This development granted radiologists, medical physicists, and doctors the technology to image the interior of the body without incisions: the CAT, MRI, and PET scans were used to target tumors non-invasively. [10]

1.1.2 Radiation Therapy Modalities

Radiation therapy can be delivered either internally by brachytherapy[b], or externally by various types of direct and indirect ionizing radiation beams. The modality used to treat the patient depends on the specific application and needs of the patient. The type of radiation therapy prescribed by a radiation oncologist depends on many factors including: the type of cancer, the size of the cancer, the cancer's location in the body, how close the cancer is to normal tissues that are sensitive to radiation, how far into the body the radiation needs to travel, the patient's general health and medical history, and whether the patient will have other types of cancer treatment.

1.1.3 Physics and Biological Effects of Radiation Therapy

Radiation therapy works because the radiation from the incoming beam is strong enough to ionize, or eject an orbital electron from an atom or molecule. When atoms or molecules in DNA are ionized, the DNA is damaged either directly by the incoming radiation, or indirectly by the creation of free radicals, as shown below in Fig. 1. When the irradiated cell cannot repair the DNA damage, the cell stops dividing or dies [6]. Radiation therapy is the physical use of ionizing radiation to induce tumor cell death, or terminate the

[b]a form of radiation therapy where a radiation source is placed inside or next to the area requiring treatment

ability for tumor cells to proliferate, which is a method proven to be effective for controlling the growth of malignant cells.

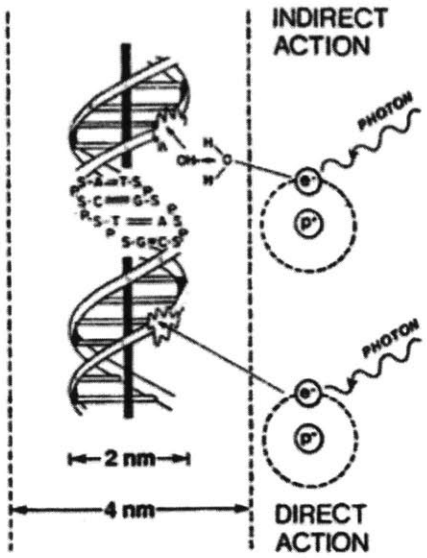

Figure 1-1: Direct and indirect action of ionizing radiation. In direct action, a secondary electron resulting from absorption of a photon interacts with the DNA. In indirect action, the secondary electron interacts with a molecule to create a free radical, which in turn damages the DNA [11].

Malignant cells have unregulated cell growth. In cancer, cells grow and divide uncontrollably, and then form malignant tumors. Depending upon the location of the tumor, cancer patients exhibit different signs and symptoms.

1.2 Treatment Planning

Once a patient is diagnosed with cancer, a team comprised of a radiation oncologist, radiation therapist, medical physicist, and medical dosimetrist develops a patient's treatment plan through a process called treatment planning. The first step in treatment planning is to create a virtual patient, a detailed set of images, e.g. CT or MRI, that show the location of the patient's tumor and the normal tissue and organ areas around it. It is

important to provide the context between the tumor and normal areas in order to optimize the dose to the tumor, while decreasing dose distributed to normal regions in order to provide a successful recovery. Medical imaging is important because it provides the medical team with an accurate visualization of the interior contents of the body such that the team can plan the geometric and radiological aspects of therapy from the medical images, radiation simulations, and optimization algorithms.

1.3 Medical Imaging

Medical imaging, a non-invasive tool that produces internal images of the body, is fundamental to conformal radiation therapy. The imaging techniques used primarily for radiation therapy are typically x-ray computed tomography (CT) scans, magnetic resonance imaging (MRI), nuclear medicine imaging (e.g., PET), and ultrasound scans [12]. Each imaging modality provides different data about the patient; thus, combining data from several modalities provides a more complete description of the patient's physical and geometric qualities. X-ray CT scans are the primary modality for image-based treatment planning, providing a clear geometric and physical model of the patient. X-ray CT has the major disadvantage since the CT data has limited contrast in showing soft tissue in the patient. MRI provides excellent soft tissue contrast, allowing for superior delineation of normal tissues from tumor volumes. Medical imaging provides information about the geometric and physical qualities of the patient.

1.3.1 Image-Guided Radiation Therapy

Improper knowledge of the patient's anatomy and position during treatment can compromise the effectiveness of the individualized dose coverage plan by imparting

insufficient dose to the target volume and/or overdose to normal tissues. The uncertainty can be caused by patient set-up or internal motion. Image-guided radiation therapy (IGRT) aims to reduce the unknown margins without compromising the clinical outcome of the radiation therapy treatment [13]. IGRT is used as a tool to detect and correct for patient set-up or motion errors, and organ movement and changes in the patient's anatomy.

IGRT is performed with ultrasound, 2D x-ray devices, and computed tomography surface imaging. It can allow for instant correction for positioning deviations and improve the precision of daily radiotherapy fractions [14]. Patient positioning, the process of aligning the patient in the treatment room with respect to the external radiation beam occurs in the operation room before radiation treatment. This step is crucial to delivering the conformal radiation dose to the tumor volume. Patient positioning occurs in the treatment room just before the patient is to receive his or her daily radiation therapy treatment, as shown below in Fig. 1-2.

Figure 1-2: Cancer patient lying on a couch with a member of the medical time in the radiation treatment room [18].

The current positioning techniques do not match the accuracy needed to perform these treatments adequately. Currently, patient positioning is a process that takes a significant amount of time and still leaves significant positioning error on the scale of centimeters, a significant margin when treated brain tumors are on the scale of millimeters. IGRT makes use of many several imaging techniques, using modalities ranging from planar imaging to fluoroscopy to cone-beam CT, and following procedures as simple as using a single set-up image or as complex as intra-fraction tumor tracking [19].

IGRT addresses patient set-up error, which can be systematic or random, which are uncertainties in patient position and beam alignment, and variation in the size, shape, and position of the tumor volume. Both systematic and random errors can arise between the pre-treatment position and planning images. The systematic error can originate at different phases during the treatment planning process, including during the data transfer from CT to the plan, or through poor registration of different imaging datasets which then propagates to the final patient positioning. The random error receives contributions from day-to-day variability, such as hydration level in the patient [13].

The current image registration modalities used for patient positioning are based on features extracted from the datasets or the intensity of the data in the image [12]. The algorithms used to interpret the features or intensity of the data are inefficient time-wise, are computationally costly, require manual intervention, and the conservative margin is usually taken at 2 cm [20].

1.4 Thesis Problem Statement

A major source of concern in radiation therapy is due to improper knowledge of the patient's anatomy and suboptimal positioning techniques, with particular interest in the location of the tumor target volume, during the course of radiation therapy. This thesis addresses the need for improving the speed and accuracy of patient positioning in medical image registration during stereotactic radiation therapy.[c] The goal of imaging is to provide a more accurate conformation of radiation dose delivery to the tumor target volume while sparing the surrounding healthy tissues. The algorithm will calculate the 6-degrees-of-freedom (DoF) transformation necessary to align the patient based on two real-time orthogonal 3D images and two projection images generated from digitally reconstructed radiographs (DRRs) generated from a 3D volume image.

2D images contain significantly less information that is present in the 3D modalities. In order to register the 2D images to the 3D volume, image fusion and registration is conducted by medical experts with algorithms that intake a significant amount of user input. Registration is a challenging task and can suffer from erroneous human input, therefore an automatic registration method is developed to be easier to use and more reliable. The goals of this thesis are:

1. To improve the accuracy of radiation dose delivery,
2. To decrease the number of preliminary scans from imaging necessary for patient positioning which thereby decreases the radiation dose delivered to the patient,

[c] single fraction radiation therapy procedure, often for treating intercranial regions

3. To determine the linear relationship between neighboring 2D projection images when multiple 6-DoF transformations are applied to a 3D volume image,
4. To develop an automatic optimization algorithm to aid in positioning of patients during radiotherapy treatments, and
5. To efficiently provide the 6-DoF transformation position shift of the patient in relation to the radiation beam.

This thesis will address four important issues that need to be addressed before image registration methods can be considered clinically acceptable:

1) first and foremost is the registration accuracy required for a specific clinical application,

2) the robustness of the alignment in terms of sensitivity of the input data,

3) the speed with which a method can be performed, and

4) the clinical feasibility in terms of image acquisition, user interaction, and interventional protocol requirements and/or acceptance.

The proposed thesis is designed to meet these four fundamental requirements, combining the advantages of the methods proposed in the past and proposing novel solutions for overcoming their drawbacks.

To limit the scope of this thesis, the assessment will focus on the use of input images of the brain: two real-time orthogonal 2D projection images from a phantom and two DRRs generated from a 3D volume image. The scope is limited to brain tumors because of the

prevalent use of stereotactic radiation therapy for brain tumors, and focused on 2D-3D registration because of its high applicability for patient positioning.

Radiation therapy has the potential to over-irradiate healthy tissue and under-irradiate tumor tissue; improving the accuracy of radiation delivery can increase and will increase the efficacy of radiation therapy and decrease the risk of adverse health effects. Reducing the duration of patient positioning will decrease error probability due to patient motion, improve the comfort of the patient during radiation therapy, and increase the treatment capacity of the radiation therapy facility with faster therapy treatment sessions.

The target audience for this thesis is the five main stakeholders in radiation therapy treatment: cancer patients, medical physicists, doctors, radiologists, and medical researchers. Medical experts who advocate minimally invasive surgeries drive the growing interest in radiation therapy. Advancing imaging registration techniques for patient positioning will guide accurate and efficient radiation therapy treatments.

1.5 Thesis Outline

The following chapter, Chapter 2, provides a thorough background of and technical issues behind image registration for radiation therapy, with a particular emphasis on current methodologies of image registration. Chapter 3 covers the methodology of the patient-positioning algorithm in detail. In Chapter 4, we present the results of the patient-positioning algorithm: the accuracy and speed as based on cancer patient data, and a sensitivity analysis of the algorithm. Chapter 5 discusses the results. We conclude in Chapter 6 by summarizing the results, describing our contributions to image registration, identifying the limitations of the algorithm, and proposing areas for new research.

2. Background

This chapter provides the background of image registration: a general introduction to the main concepts, current developments in the field of 2D-3D rigid-body image registration applied specifically to radiation therapy, and an outline of our registration approach. A summary of current image modalities and image registration techniques that are used most frequently is presented. Then, technical challenges behind image registration are identified. Lastly, a new approach to 2D-3D image registration is introduced.

2.1 Patient Positioning

Precise alignment of the patient relative to the radiation beam is important in simulation and daily treatments. The accuracy and reproducibility of positioning are strongly dependent on the anatomic region involved and on the positioning aids used to place the patient in exactly the same position as in treatment planning [14]. Positioning is assisted with patient immobilization casts (e.g., body molds and head masks), or temporary skin marks, implanted metal pellets, or tattoos to realign the patient, but variations as much as 10 mm may occur between the visualized and the actual position [14]. These patient positioning tools are used to assist in developing images of the patient.

Patient positioning developed from 2D-3D image registration, the alignment of a 2D projection image to a 3D volume set, is a type of image-guided radiation treatment (IGRT). The main objective of IGRT is to efficiently provide accurate information about patient anatomy to assist in treatment planning for high precision, conformal dose to the target tumor volume, and sparing of adjacent neighboring tissues.

2.2 Medical Image Modalities

Medical imaging provides detail about the anatomy of interest. Imaging data can be produced from imaging modalities such as x-ray computed tomography, magnetic resonance imaging, positron emission tomography, single photon emission computed tomography, and ultrasound imaging. There is no one modality that can fully provide all geometric, physical, and functional information about the patient; rather, the combination of the unique imaging strength of each modality can provide the necessary data of anatomy, tissue contrast, organ contrast, volumetric information, functional qualities to the medical team, depending on the particular need [12].

2.2.1 Computed Tomography Scans

Computed tomography (CT) imaging data is generated from x-rays. The CT scan is produced when x-ray tubes and detectors rotate around the patient at predetermined angles. The CT scans measure the physical parameters of x-ray absorption, density and average atomic number, and contrast distribution to show the anatomy, mineral content, and movement of contrast material, composed of an element of high atomic number, in patients [15].

The attenuation of an x-ray traversing a thin slice of homogeneous material is described by Eq. 2.1:

$$I = I_0 \exp(\mu d) \tag{2.1}$$

where I_o is the input intensity, μ the coefficient of linear attenuation of the material, and d the traversal distance of the x-ray [16].

To extrapolate to the human body, which consists of a numerous combination of different structures with different attenuation coefficients, Eq. 2.2 represents the human body in the same form as shown above in Eq. 2.1:

$$I = I_0 \sum_i \exp(-\mu_i d_i) \tag{2.2}$$

where I_o is the input intensity, μ_i the coefficient of linear attenuation of structure i, and d_i the traversal length of structure I [13].

The pixel values in the CT scan correspond to the mean attenuation of the imaged tissue on the Hounsfield scale. Hounsfield values, H, are defined in Eq. 2.3 [16]:

$$H = \frac{\mu - \mu_{water}}{\mu} \cdot 1000 \tag{2.3}$$

The Hounsfield values H typically range [-1000, 3000] to represent the densities μ [air, metal] in the human body. CT scans are the primary dataset used to develop the geometric and physical model of the patient in radiotherapy treatment planning when determining the dose distribution. The geometric models derived from the CT images are used to define and delineate anatomic structures, target volumes and to aid in radiation beam placement and shaping. Distortions in the anatomical geometry of the patient are not of major concern to CT scans. The major disadvantage of CT scans is the limited soft tissue contrast, which can hinder accurate normal from atypical tissue discrimination. [12]

Multiple CT scans taken of the same object at different locations can be stacked to generate a 3D volume image such as the reference volume image used in this thesis.

2.2.2 Digitally Reconstructed Radiographs

Digitally reconstructed radiographs (DRRs) simulate x-ray imaging and are reconstructed from medical tomography data sets of a patient either from a visual comparison of the planning images versus those of the treatment stage, or from automated registration algorithms. In our case, DRRs are generated from a series of 2D x-ray CT images and are derived from the law of attenuation absorption [17]. The resulting 2D images of DRRs simulate normal x-ray images but are only approximations of attenuation [16].

DRRs can be computed with different algorithms from CT data. The most straightforward and frequently used method is a ray-casting algorithm, which does not consider lighting circumstances and reflections but rather finds the intersections of a ray with all objects in the scene, as shown below in Fig. 2-1.

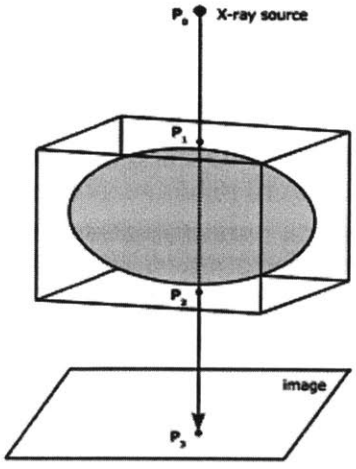

Figure 2-1: DRR generation. A single ray originating at P_0 in the x-ray source enters the volume at P_1 and exits at P_2 to create the pixel P_3 in the image [16].

Additional algorithms such as shear warp factorization and hardware texture mapping for DRR generation exist. The various DRR algorithms have different approaches to predicting the approximations and may feature the option to conduct interpolations or estimate non-linear attenuation. The DRR images used in this thesis are generated from raycasting.

2.2.3 Magnetic Resonance Imaging

Magnetic resonance images are produced from MRI machines that use a powerful magnetic field to align the magnetization of particular atomic nuclei in the body. The radiofrequency fields are systematically changing the alignment of the magnetization, which causes the nuclei to produce a detectable precessing magnetic field. MRI is used to provide excellent contrast of soft tissue, which provides clear discrimination between normal tissues and tumors. The MRI measures the concentration of net spin nuclei, such as ^{1}H, and the relaxation parameters as a form of frequency shift to show the anatomy of tissues, free water content, and flow concentration of some molecular species [15]. Pulse sequences allow enhanced image contrast or the suppression of specific tissues. An additional advantage of MRI is its ability to produce images along sagittal and coronal planes, offering better visualization of certain tissues. The drawbacks include the greater susceptibility to spatial distortions, intensity artifacts, and image intensity values that do not correspond to electron or physical density [21, 22].

2.2.4 Nuclear Medicine Imaging

Two instances of emission computed-tomography based on nuclear medicine imaging are positron emission tomography (PET) and single-photon emission computed

tomography (SPECT) which image the transport and concentration of biologically active tracers. An example of a radioactive tracer for PET is 18-F, and for SPECT is 99m-Tc. The resulting image is best at providing information about physiology, especially about tumor metabolism, receptor site concentration and flow, and partial-volume tissue function [15]. For patient monitoring, nuclear medicine imaging has proven useful for assessing the response of the patient to radiotherapy. The use of PET is limited because of the high cost of cyclotrons needed to produce the radioactive tracers. The patient ingests or is implanted with the source of ionizing radiation that specifically target the organ of interest [23].

2.2.5 Ultrasound

Ultrasound imaging uses cyclic sound pressure at a high frequency to measure acoustic impedance mismatch and sound velocity and attenuation to produce images [15]. Ultrasound images tissue structural characteristics and blood flow well, but does not provide clarity of internal geometric structures. The major advantages of ultrasound are that images are produced in real-time, the required apparatus is relatively small, and imaging does not involve ionizing radiation. A disadvantage of ultrasound is that not all regions of the body, such as the brain and lung, can be imaged effectively due to signal loss at large tissue density changes such as at tissue-bone and tissue-air interfaces [12].

2.2.6 Summary of Imaging Modalities

Medical imaging can be conducted with the following imaging modalities: computed tomography scans, digitally reconstructed radiographs, magnetic resonance imaging, nuclear medicine imaging, and ultrasound. These images are used in the image registration process to assist during patient positioning.

2.3 Image Registration Process

Image registration is the process of establishing point-by-point correspondence between two (or more) same or similar images of a scene taken at different times, from different viewpoints, and/or by different sensors [24]. The goal of image registration is to geometrically align the two images, which differ due to the aforementioned imaging conditions. The final information from image registration is crucial in patient positioning in which the transformation function mapping the two images together is sought.

The input image undergoes a transformation and maps to a homologous dataset representing the base image, the primary dataset as shown in Fig. 2-2.

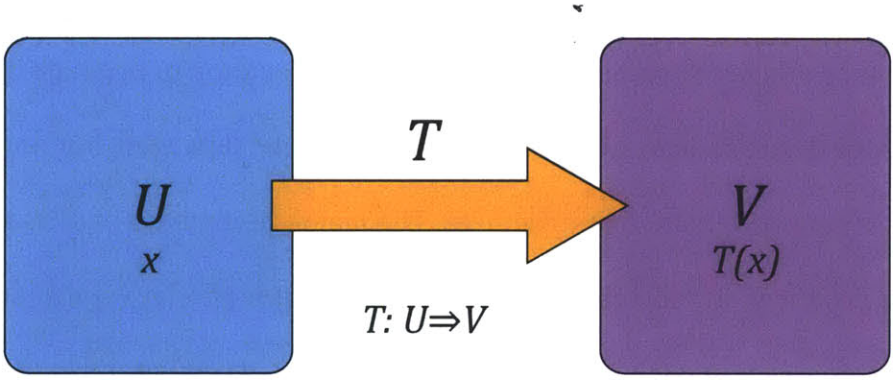

Figure 2-2: Mapping Image U to Image V by transformation T.

The essential elements of image registration are: 1) reference/base image(s) V, 2) input/target image(s) U, and 3) transformation function T that maps the reference image to the input image.

The general approach of 2D-3D image registration methods to assist with patient positioning is [25]:

1. Preprocess the two datasets (the reference image and the input image) to have homologous features
2. Select homologous features in the two datasets
3. Conduct feature correspondence and enumerate with a metric that measures the degree of similarity
4. Determine transformation function between the reference image and the input image
5. Repeat steps 3 and 4 by resampling at new positions, and
6. Optimize by maximizing the similarity metric.

The common initialization step is to preprocess the datasets so they can be interpreted in the same domain (e.g., resolution, size), identify the metric that measures the degree of similarity in the images, enumerate the position, and then resample until the similarity between the images is maximized.

2.4 Transformations

The transformation functions examined in this thesis are described as rigid-body, linear, affine, and with six degrees-of-freedom.

With target volume encapsulated in rigid anatomy, such as in the skull or pelvis, the motion can be appropriately represented as a rigid body transformation. In rigid body transformation, the anatomy can only undergo motion along three independent axes, allowing for three rotations and three translations. The set of three rotations *(θx, θy, θz)* and three translations *(tx, ty, tz)* is referred to as 6 degrees-of-freedom (DoF), as shown on the phantom head in Fig. 2-3.

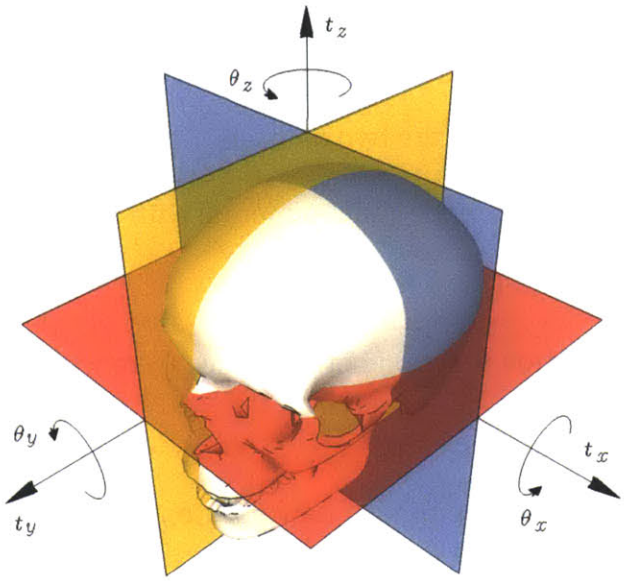

Figure 2-3: Six degrees-of-freedom composed of three rotations *(θx, θy, θz)* and three translations *(tx, ty, tz)* on a skull.[d]

Non-rigid, or elastic, systems that are capable of being locally warped, and systems that suffer from image distortions or poorly calibrated imaging devices require additional DoF to identify the spatially variant transformation involved. The additional DoF required to register this data properly include anisotropic scaling. This algorithm will assume a rigid body system of 6 DoF.

Rigid body transformations can be represented as linear transformations of translations and rotations. The transformation is an affine map where straight lines are preserved by definition. The conversion from one frame of reference to another can be represented as a transformation vector undergoing a change in perspective. Once the two frames of references are known, the transformation matrix can be easily determined. The linear transformation T mapping x to x^1 is shown below in Eq. 2.4.

$$x' = Tx \tag{2.4}$$

[d] Courtesy of Bryan Haddon

The transformations T can be represented as individual matrix transformations that represent translations and rotations. The three translations of perturbations *(tx, ty, tz)* can be calculated together as *T(tx, ty, tz)* in Eq. 2.5. The rotations are represented separately as rotations about their respective axes: $T(\theta_x)$, $T(\theta_y)$, *and* $T(\theta_z)$, as calculated in Eq. 2.6, 2.7, and 2.8.

$$T(tx, ty, tz) = \begin{bmatrix} 1 & 0 & 0 & 0 \\ 0 & 1 & 0 & 0 \\ 0 & 0 & 1 & 0 \\ tx & ty & tz & 1 \end{bmatrix} \tag{2.5}$$

$$T(\theta_x) = \begin{bmatrix} 1 & 0 & 0 & 0 \\ 0 & \cos\theta_x & \sin\theta_x & 0 \\ 0 & -\sin\theta_x & \cos\theta_x & 0 \\ 0 & 0 & 0 & 1 \end{bmatrix} \tag{2.6}$$

$$T(\theta_y) = \begin{bmatrix} \cos\theta_y & 0 & -\sin\theta_y & 0 \\ 0 & 1 & 0 & 0 \\ \sin\theta_y & 0 & \cos\theta_y & 0 \\ 0 & 0 & 0 & 1 \end{bmatrix} \tag{2.7}$$

$$T(\theta_z) = \begin{bmatrix} \cos\theta_z & \sin\theta_z & 0 & 0 \\ -\sin\theta_z & \cos\theta_z & 0 & 0 \\ 0 & 0 & 1 & 0 \\ 0 & 0 & 0 & 1 \end{bmatrix} \tag{2.8}$$

The transformations in this thesis are taken to be affine. Affine transformations are a subset of projective transformations. In a projective transformation, quadrilaterals map to quadrilaterals, straight lines remain straight, and parallel lines map to parallel lines.

Affine and rigid-body transformations can be conveniently represented using homogeneous matrices. Affine transformations allow for a fast calculation of linear transformations.

Linear transformations must satisfy two requirements: i) preservation of scalar multiplication, and ii) preservation of addition. The displacements of the input image from the base image will be very small, so linear approximations can be made.

Thus, the transformation applicable to this thesis can be represented in a matrix form of linear transformations as shown below in Eq. 2.9:

$$B = T(tx, ty, tz, \theta x, \theta y, \theta z)A \tag{2.9}$$

where the input image B maps to reference image A by undergoing transformation T.

2.5 Current Image Registration Modalities

The current image registration modalities are based on features extracted from the datasets or the native grayscale data. The features are typically geometric structures such as homologous points, lines, surfaces, or a combination that are either manually placed fiducials and stereotactic frames, or selected from anatomical features or extracted surfaces [12].

Applications of image registration are change detection, image fusion, target recognition, target localization, depth perception, image mosaics, and motion estimation. The image registration modalities described below account for rigid anatomy and are commonly geared for the six degrees-of-freedom: three rotations and three translations. The methods described below are referred to as 2D-3D dataset registration methods,

which correlate a 2D reference position with a virtual 3D dataset. In medical imaging, image data from the same patient is taken at different points in time or by different detectors. The challenge in medical image registration is that the data from different points in time may be slightly modified due to deformation of the subject, such as breathing or anatomical changes.

Current image registration methods assume that two sets of features, e.g. fiducials or tattoos, in the reference and input images can be well represented. The methods find the pairwise correspondence between them using their spatial relations or various descriptors of features [24].

2.5.1 Feature-based Registration

In feature-based registration, anatomical features of the base and input images are an object used in the field of view which appears in the image produced, e.g. implanted metal pellets skull are treated as landmarks and used to compute and minimize the mismatch between the datasets. Various automated techniques or manual selection is used to extract the anatomical features from the image. While early algorithms were based on expert selection of points, newer algorithms are automated in finding corresponding features between the images [24]. Then, the degree of mismatch between the two datasets corresponding to the features is computed as the sum or average of the distances between the two images. The disadvantage of feature-based registration is hefty pre-processing of the data to precisely select the features [12]. Additionally, problems caused by incorrect feature detection or by image degradations can arise since physically corresponding features can appear dissimilar due to the different imaging conditions and/or due to the different spectral sensitivity of the sensors, leading to degenerate solutions [24].

2.5.2 Intensity-Based Registration

Another type of dataset registration is intensity-based registration. In intensity-based registration, intensity patterns in the entire grayscale data are extracted and compared via correlation metrics. A method that is being widely developed for intensity-based registration is a mutual information (MI) based metric, a measure of statistical dependency between two data sets [24]. This metric measures the level of redundant information in the input and target datasets as shown below in Eq. 2.10:

$$MI(X,Y) = H(Y)-H(Y|X) = H(X) + H(Y)-H(X,Y) \tag{2.10}$$

where $H(X) = -E_x(log(P(X)))$ represents entropy of random variable and $P(x)$ is the probability distribution of X. The pixel values are scalar values representing the intensity.

The joint probability distribution H collects a histogram of the grayscale pairs from the datasets at each instance of coordinate transformation estimations. A reduction of MI means a smaller probability of predicting one homologous pixel value from one dataset to the other. This registration method is good at handling images of different image modalities, such as homologous CT and MRI datasets. The disadvantage of intensity-based registration is that is computationally intensive. Additional methods are implemented, such as a coarse-to-fine resolution strategy and spline pyramids, to speed up the MI process. Another disadvantage is false point matching due to poor image quality and by complex nature of the image degradations, leading to poor robustness and reliability [12, 24].

2.6 Optimization of Image Registration

Once a metric to measure the similarity or dissimilarity of image registration is selected, an objective function measuring the metric is created and then optimized to find

the best alignment of the two image datasets. Typically, extrema define the most optimal solution is created by the similarity metric. Thus, the alignment of the best match between the images is when the objective function is maximized or minimized.

Two common techniques to maximize the objective function are gradient functions and non-gradient functions. Gradient functions find the rate of change to indicate the direction towards the extremum. Non-gradient functions execute a method of local search by evaluating the objective function at select locations.

Previous and current approaches often rely on a good initial estimate of the pose parameters, the position and orientation, before the optimization algorithm refines the parameters until extrema are found. An example optimization algorithm is the iterative closest point, which iteratively calculates the distance between two shapes with for example the least squares method until minima are found. This procedure often leads to registration errors due to poor initial pose parameters and is prone to local minima traps [26]. Additionally this optimization method requires the greatest time in registration and has a problems caused by its iterative nature and objective function.

2.7 Challenges of Current Image Registration Method

The objective of image registration is to be able to align the input image with the base image by applying a spatial transformation. The goal of 2D-3D image registration is to align the input image to the base image such that the alignment of the patient with respect to the radiation treatment beam in the treatment room can be calculated. In medical imaging patient positioning, it is necessary to know only the relative transformation and position between the beam and the patient.

Image registration is comprised of two coupled problems: the correspondence problem and the pose problem [27]. Solving the correspondence problem consists of finding matching image features and model features. If the camera pose is known, one can relatively easily determine the matching features. Looking at the model from the point of view defined by the camera pose, one defines the model features that are observed to be close to the features of the new image. Solving the pose problem consists of finding the rotation and translation of the camera with respect to the model. Given matching image and model features, one can easily determine the pose that best aligns those matches.

The classic approach to solving these two coupled problems has been a hypothesize-and-test approach, in which (a) guesses are made about matches between a few image features and a few model features, (b) the camera pose is computed using these matches, and (c) the remaining model features are projected on the image and a measure of the quality of their superposition with image features is computed. This process is repeated for all reasonable groups of matching guesses, and the correct camera pose and superposition are chosen from among those that provide the highest measure of superposition. However, this type of approach is generally expensive for complex models and images [28].

In medical imaging, image datasets of the patient are taken at different points in time, by different detectors, or by different imaging modalities. One challenge in medical image registration is that the data from different points in time may be slightly modified due to deformation of the subject, such as breathing or changes in anatomical structure such as weight loss. The variance in different imaging modalities by their innate characteristics spawns the challenges mentioned previously. Another challenge is the initialization of the detectors: the same detector day-to-day, or different detectors can

cause small but significant discrepancies in dataset values.[e] Image noise is another challenge, and can be a result of various reasons, from backscatter of implanted metal pellets to patient motion, to poor initialization of the detector.

The varying quality of images that display a representation of the internal organs, tissues, and function of the patient present a level of uncertainty, which is supplemented by more uncertainty from the image registration process. The spatial and temporal differences between the images may be affected by any single or combination of the issues identified above.

2.8 Outline of the Registration Approach

Registration algorithms can be decomposed into three components: i) the similarity measure of how well two images match, ii) the transformation model, and iii) the optimization process that varies the parameters of the transformation model to maximize the matching criterion [29]. Current classical approaches to image processing allow for improvement in all three attributes in both time and accuracy.

In order to provide accurate 6 DoF patient positioning, our approach to develop an efficient 2D-3D image registration process will begin by understanding the challenges and scope of the task at hand. 2D-3D image registration is the process of aligning a pair of orthogonal 2D images: U_c is the coronal view and U_s, is the sagittal view of the patient with the 3D volume image V, as shown below in Fig. 2-4, which is the specific case of mapping shown previously in Fig. 2-2.

[e] Detectors are subject to change based on the operating temperature, pressure, humidity, etc.

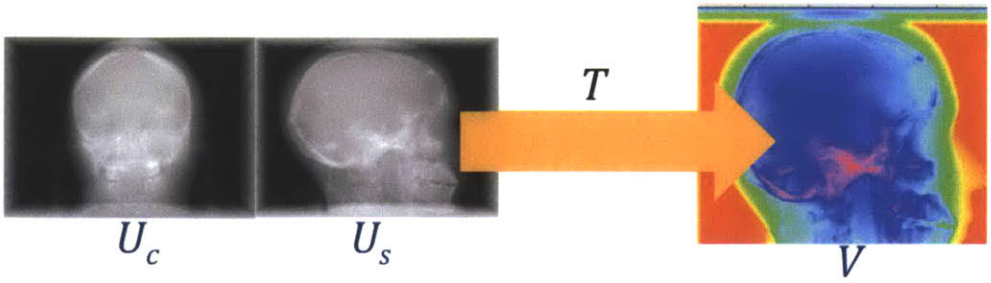

Figure 2-4: 2D-3D Image Registration of input images U to base volume image V under transformation T.

The overall goal is to derive the coordinate transformation that maps the input image dataset points to the base image dataset. The two image datasets have different scenes: the patient's anatomy may have changed slightly, the image datasets at hand are taken at different times by the detector, and the gantry-to-patient positioning are initialized differently by the hardware.

The focus of my approach is to conduct 2D-3D image registration given the three essential elements: a base dataset that is the volume image, the input dataset that is an orthogonal pair of 2D images, and transformation T that is linear by definition and has six degrees-of-freedom *(tx, ty, tz, θx, θy, θz)*. The goal is to return a 6-DoF geometric transformation bridging the base dataset pose and the input dataset pose that best specifies the pose of the images for the application of stereotactic radiotherapy. The image registration will be geared toward stereotactic radiotherapy. In this case where the tumor volume is in the head, the bones act as a reliable frame of reference to make stereotactic calculations possible. The reason a pair of 2D images and DRR projections are used in this algorithm is because they are the common datasets collected from radiotherapy treatment

planning since they together provide information about the geometric anatomy and tissue delineation in the patient.

The selection of a similarity metric should contain elements of the dataset that uniquely represent the relative coordinates of and effectively characterize the image. The similarity metric was expected to meet execution speed requirements, show robust performance, and be accurate. Current image registration modalities have many limitations, as described above. Our choice of the metric depended on the examined image modalities, excluding possible distortions in the images to be registered and implementation issues.

We wanted to eliminate manual point selection by a user from our procedure, as it introduces one of the largest sources of error in image registration [14, 24]. Execution played a large role in our decision to select this similarity measure. We elected to use all of the points in the image, and then select a subset of the image to investigate; it is possible to reliably characterize the image without using all available intensity information provided. A stochastic sampling approach was considered, but because of the small size of the images, it was possible to sample all data points in a timely manner. The generality of the shape distribution method allows it to be used for all intensity-based image modalities. Thus, the shape distribution method, which is described briefly below and in detail in the following chapter, was developed to meet these requirements.

2.9 Shape Distribution

The shape distribution method of calculating shapes is possible without using pose registration or feature correspondence, two costly processes in classical image registration methods. The idea is to represent the signature of an object as a shape distribution sampled

from a shape function measuring global geometric properties of the object [30]. The attributes, such as the distance between two selected points, define a variable space by generating distribution histograms of the attribute [30].

The shape function is used as an alternative to the classic approach of intensity-, point-, or surface-based algorithms because it is an affine-invariant, robust method. The need for landmark features has been eliminated because landmarks cannot be selected accurately in x-ray images and are a major factor in registration errors. The shape distribution method is insensitive to noise, topology, and is quick and efficient. This method allows for an arbitrary 2D or 3D model to be transformed into a parameterized function that is easily analyzed. The shape distribution method does not label the image from a prior knowledge set, but is relatively positioned between input data points.

The shape function is the operation that creates geometric histograms called shape distributions that are unique to each image, creating a representative signature as sampled over the given domain. The shape distribution concept was developed by Robert Osada *et al.* for representing 3D models as a two-dimensional probability distribution sampled from a shape function measuring a strategically selected geometric property of the 3D model [30]. Presented was a generalization of the Shells method, the representation of a 3D model as a distribution of distances of surface points from the center of mass, by generating a histogram of distances between pairs of points on the surface of a model. The shape function method allows for the characterization of a defined shape attribute and identifying the distribution of that attribute.

To give an example, the *D2* shape function shown below in Fig. 2-5 is defined as the function represents the distribution of Euclidean distances between pairs of randomly

selected points on the surface of a 3D model. The *D2* descriptor is a one-dimensional, rotation-invariant representation of 3D shapes. The *D2* shape distribution was normalized to be invariant to scale.

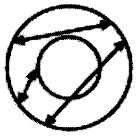

Figure 2-5: The *D2* Shape function samples the distance between two randomly selected points on the surface of the object.

In a random sampling distribution, the *D2* shape function creates shape distributions as the probability of finding an element of the object at that given distance. In each *D2* shape distribution plot below in Fig. 2-6, the horizontal axis represents distance, and the vertical axis represents the probability of the distance between two points on the surface of the labeled solid object.

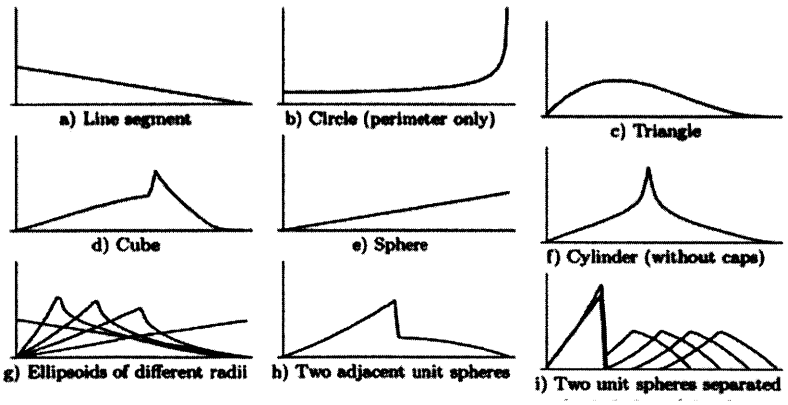

Figure 2-6: Distributions of the *D2* shape function as evaluated on different input objects.

The shape distribution concept has been adapted to fit the objectives of our image datasets. Osada had limited the shape distribution to navigate a domain of uniformly

distributed shapes and by sampling a random subset of points to create a position-invariant descriptor of a 3D model. We had extended the shape function concept to navigate the full domain of the images in order to provide the pose of the 3D model.

2.10 Objective Function and Optimization

To select the optimal transformation bridging the reference image and the input image, automatic optimization procedures were considered. We avoided methods known to be at fault to local extrema registration errors. Mathematical morphology and image processing techniques are used to maximize the shared information between the DRRs and the input images to align the patient to the planned position.

The nature of the characteristic datasets output by the shape function naturally led to the selection of a similarity metric based method, so covariance was selected as the ideal function to identify the combination of transformations of highest correlation to identify the 6 DoF.

Optimization of the objective function was expected to find the most probable 6-DoF transformation that aligned the 2D input images with the 3D base volume.

2.11 Summary of Background

The objective of stereotactic image registration is to derive a coordinate transformation that maps homologous points from one dataset to the other. Current registration methods are feature-based where homologous points on datasets are matched, or intensity-based where intensity patterns in the datasets are matched. The current registration methods tend to be time consuming and subject to registration errors.

Common optimization methods that follow the registration methods find the extrema to the defined similarity metric as defined in the registration method. One commonly used optimization method is the least squares method, which may suffer from local extrema traps.

We have developed an image registration modality that addresses the disadvantages presented by current image registration and optimization methods.

3. Registration Algorithm

This chapter provides a detailed description of the methodology of the image registration algorithm. In Matlab, we developed an efficient patient-positioning tool that can be used to accurately measure and calculate the transformation needed to aid the alignment of the radiation beam with the patient in the treatment room. We aim to recover the six degrees-of-freedom rigid-body transformation between a 3D model volume and a pair of orthogonal 2D images without the use of fiducials or other landmark features.

In this chapter, we introduce the steps of data preprocessing, characterization of images by shape distribution, the objective function, and optimization to provide the most statistically likely 6-DoF transformation. Details of its implementation are described. The algorithm interprets the evaluated transformation as a linear combination of each individual transformation represented by the shape function. Then, we compare the shape distribution approach against two different approaches. Lastly, we give a general overview of the registration algorithm. The results of the algorithm follow in Chapter 4.

3.1 Registration Algorithm Outline

The 2D-3D registration process can be categorized as two different periods that are calculated at two different times as offline calculations and online calculations. During offline calculations when the patient is not in the treatment room for radiation therapy, CT data is collected and a 3D volume image of the region of interest patient is created. The 3D volume model data is preprocessed for image registration, a domain is defined by a series

of small-scale transformations, and the volume is transformed across this domain. Shape distributions of orthogonal projections of the transformed volumes are created to form the sparse base transformation set *SV* that corresponds to each small-scale transformation. These steps can all be conducted offline.

When the patient is in the patient room ready for receiving therapy treatment, online calculations are taken: a pair of orthogonal images *U* of the patient are taken (e.g., x-rays), shape distributions *SU* of *U* are created, and then these distributions are correlated against *SV*. The correlations *C* are optimized to output a 6-DoF transformation that most accurately maps *U* to *V*, which is also known as the relative transformation that optimally aligns the patient to the beam. The full image registration algorithm diagram is shown below in Fig. 3-1. The offline steps are shown in Fig. 3-2.

Data preprocessing allowed for *U* input data set and *V* the base data set to be defined in a common reference coordinate system. *V* is defined as the base image intensities defined over domain $\Omega_v \subset \Re^3$. The input image intensities is defined as $U_{I,j}(u_{I,j})$ defined over domain $\Omega_{I,j} \subset \Re^2$ and by $u_{I,j} = 1,2...N_I$ where N_I is the number of intra-interventional image intensity sets. In our case we have a pair of orthogonal images so N_I is 2.

The spatial transformation *T* that aligns the projections of *V*, $P_j(V^T(v))$, with the orthogonal 2D images *U* is defined in Eq. 3.1 as:

$$P_j(V^T(v)) = U_{P,j}^{TP}(V_{P,j}) \Leftrightarrow U_{I,j}(x_{I,j}), \bigcap j \tag{3.1}$$

where $(V^T(v))$ denotes the transformed base data set and P_j defines projection transformations that map N_I-2D domains $\Omega_{I,j}$ with the 3D coordinates $v \in \Omega_v$.

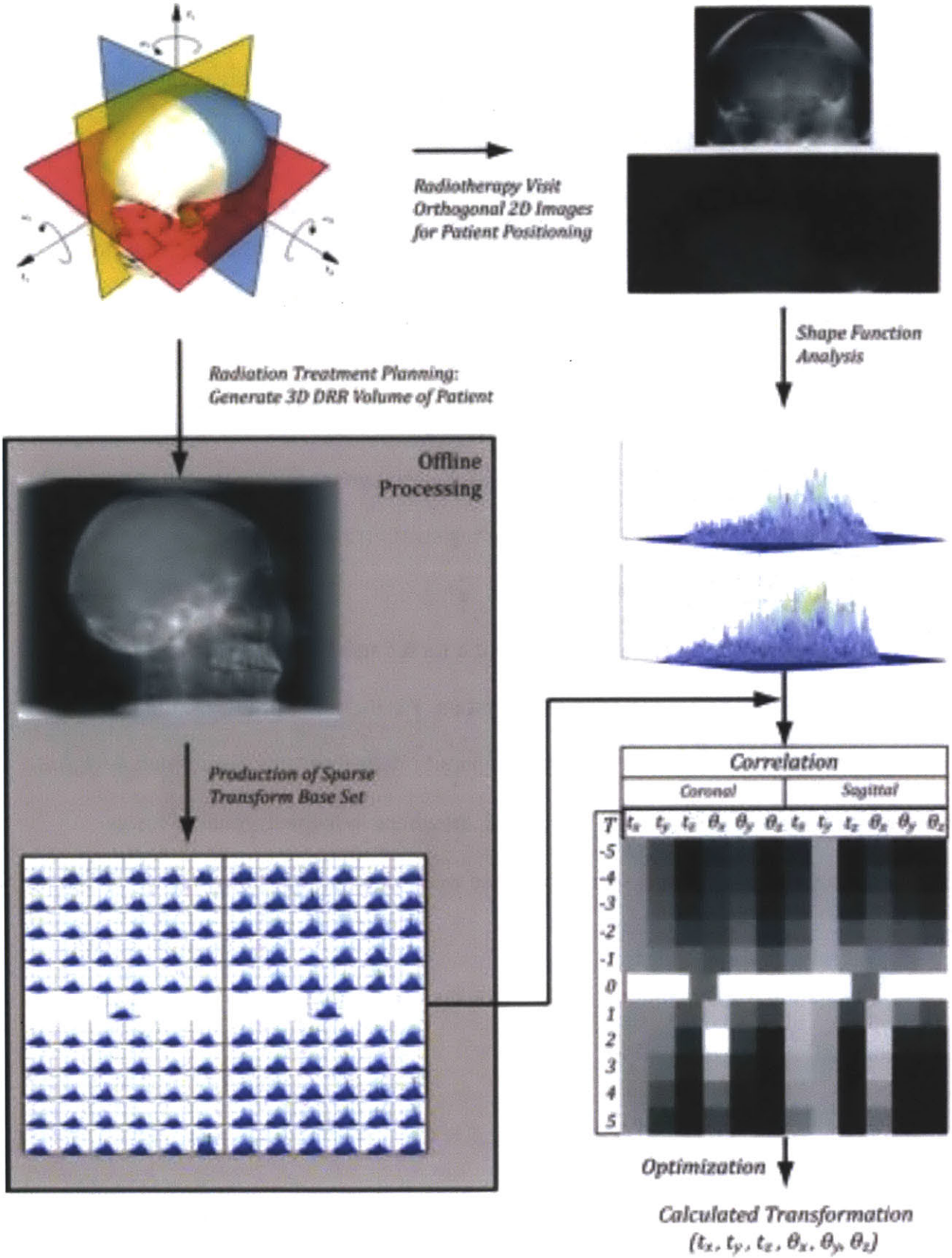

Figure 3-1: Shape distribution image registration algorithm.

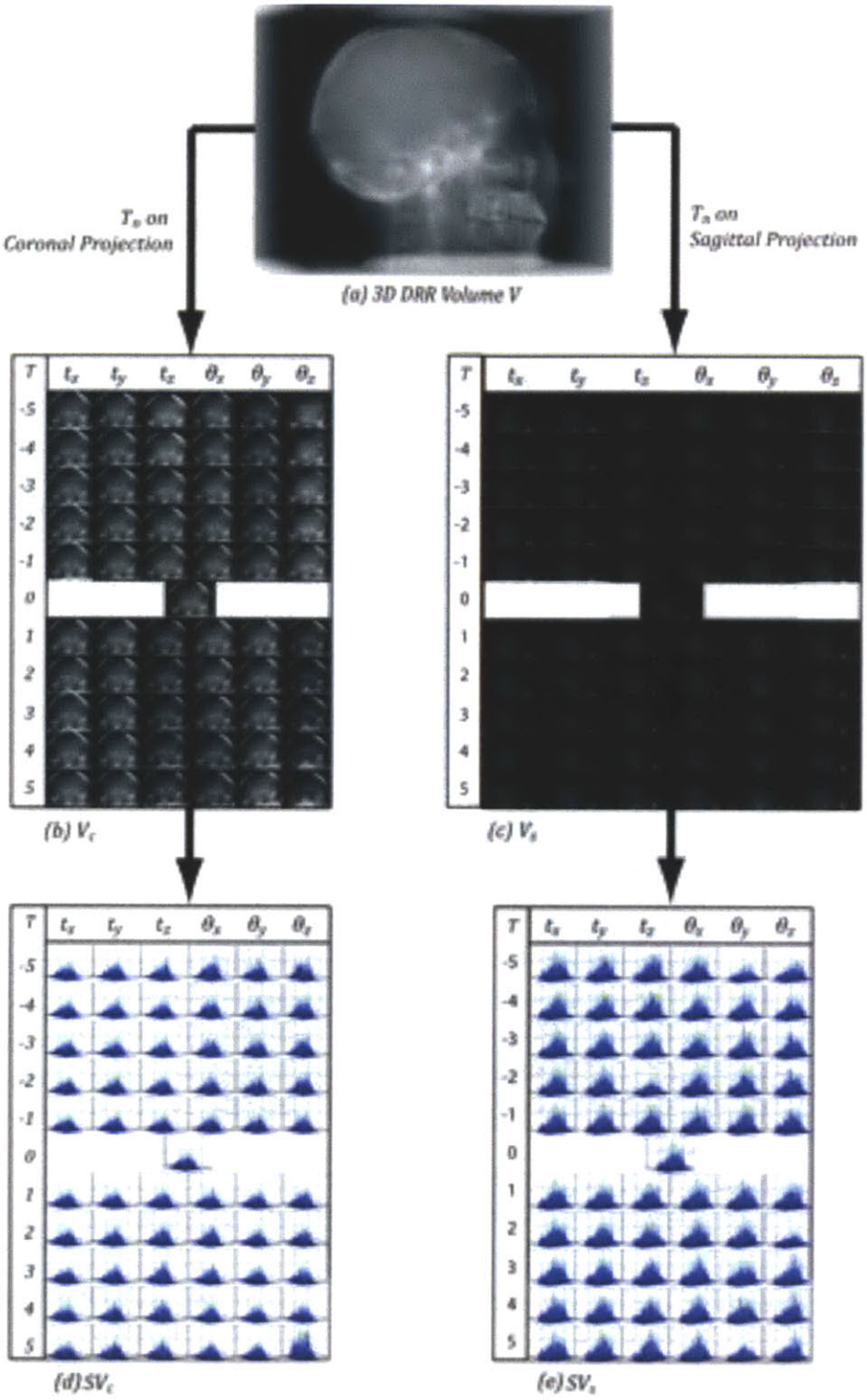

Figure 3-2: Offline Calculations: 3D DRR Volume *V* (a) is used to generate a series of transformations of the coronal (b) and sagittal (c) projections. The shape function determines the characteristic shape distribution for each of the projection images, producing a sparse transformation base set for both coronal (d) and sagittal (e) projections.

3.2 Data Preprocessing

The first step of the algorithm is to preprocess the input data and base data. Both the 2D projection images and the 3D reference volume are images taken of the same phantom. The data is filtered to remove noise, and then the data is parameterized to map the intensity values from U to V. Data preprocessing is a multi-step approach.

Shown below in Fig. 3-3 is the coronal projection V_c (left) and sagittal projection V_s (right) of the 3D reference volume composed of 152 2D-CT slices from which the DRR volume V is generated. The DRR projections generated from the 3D volume image were initially of resolution 1024 x 768 pixels. The isocenter of each image in both image datasets were saved. Each pixel in the DRR projection images represents 0.5098 mm x 0.5098 mm.

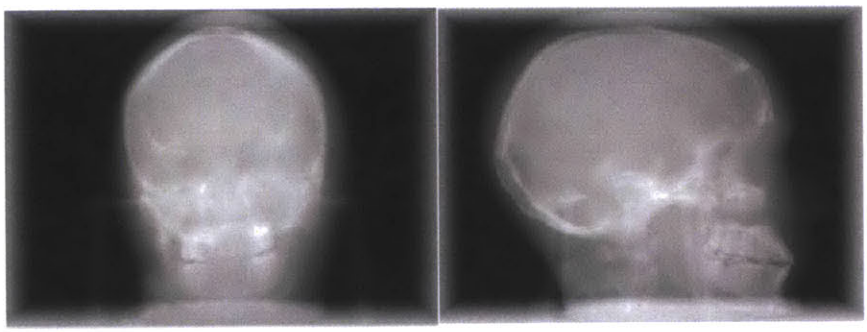

Figure 3-3: Orthogonal pair of DRR projections derived from the 3D volume image: coronal projection (left), sagittal projection (right).

The data points outside of the head were cropped (e.g., the air gap surrounding the head and the head brace) to reduce memory and the computed domain, as shown below in Fig. 3-4. The following steps of the algorithm necessitate the preservation of the data points containing bone information, so the bone matter around the brain was preserved.

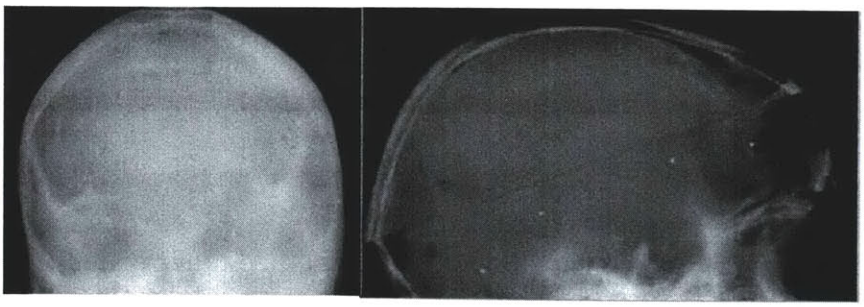

Figure 3-4: Orthogonal images of *U*, cropped and values adjusted.

Noise in the images is removed with image filters. The noise in the images is due to the inevitable differences of a pixel to any other in the matrix caused by unavoidable non-uniformity in the realization process [31].

After data preprocessing, the values of the two image modalities span the same anatomical domain space and intensity range, and is successfully prepared for the following steps.

3.3 Defining Permissible Transformations

At small-scale changes, 6-DoF rigid-body transformations can be represented as a combination of independent transformations. The property of additivity in linear transformations as shown below in Eq. 3.2 allows us to treat the 6-DoF transformation T as a six individual transformations for each DoF in the domain space that maps the 2D projection images to the 3D volume image [32].

$$T(dx + dy + dz + \theta x + \theta y + \theta z) = T(dx) + T(dy) + T(dz) + T(\theta x) + T(\theta y) + T(\theta z) \tag{3.2}$$

Taking the transformation at the small scale to be linear allows us to treat the transformations as affine. A tendency for the values of the variables to linearly increase or

decrease in tandem implies a linear correlation between the variables. When there is no correlation between variables, there is no tendency for the values of the variables to change in unison. In addition, the relationship between variables may be non-linear, meaning variables that are uncorrelated are not necessarily deemed independent.

3.4 The Shape Distribution Metric

The objective function spans the domain defined by the reference images *V* and input images *U*. This algorithm will evaluate the objective function as defined by the shape function. It is necessary to establish the shape function such that information about the pose is not lost during the creation of the image descriptor. The objective function will be evaluated in the subsequent optimization step to identify the transformation relationship between *U* and *V*.

In our algorithm, we defined a novel shape function *F(I)* that samples the image domain space *I* as a distance from the isocenter and the intensity of the sampled pixel, as shown below in Fig. 3-5. This full domain is sampled to obtain the unique contribution of each point in the image to the complete shape distribution characterizing the image. The sampling of the full image domain does not compromise the efficiency of the algorithm because the cropping of the background already reduced the size of the image.

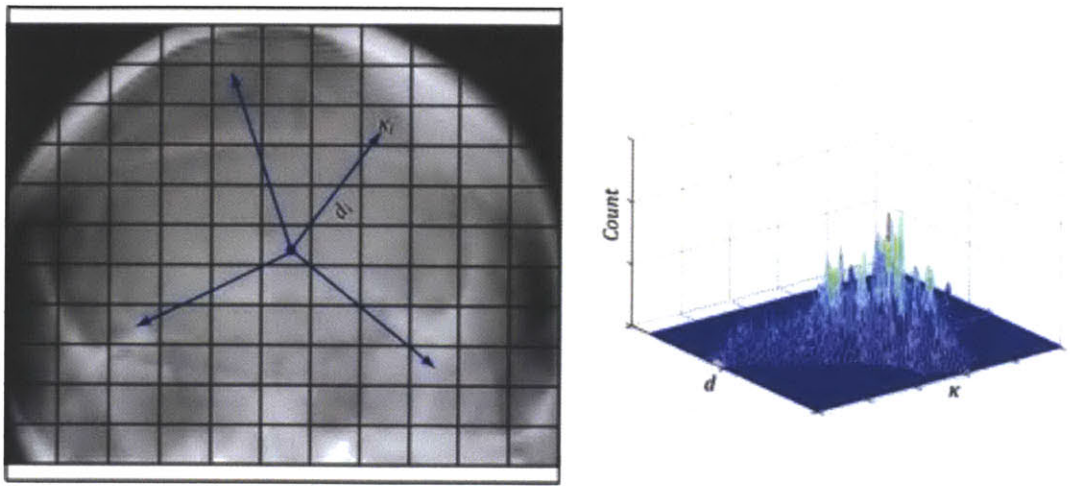

Figure 3-5: Shape function *F(I)* samples the distance from the isocenter d_i and the pixel intensity κ_i of each pixel in the image *I* (left). The shape distribution *S(I)* characterizes *I* as a histogram of d_i and κ_i (right).

The idea to represent the signature of an object as a shape distribution sampled from a shape function measures the global geometric properties of the object [30]. The shape distribution defines a variable space by generating distribution histograms of the attribute. The attributes, such as distances and angles between select points, are selected strategically to meet the needs of the problem [30]. We have defined a shape function to span a domain characterizing an image by both its pixel intensity value and distance from the isocenter that uniquely characterizes each image.

Our shape function *F(I)* samples the full domain of *I* to locate pixels of high intensities representing high-density regions, e.g. bone. The bone matter is the feature-of-interest because of its anatomical rigidity allowing for stereotactic measurements and large presence in the domain space encompassing the tumor volume-of-interest, making it a consistent and reliable characteristic attribute in each image. In addition, the reduction of the shape distribution *S(I)* by eliminating the detection of lower intensities reduces computational requirements and provides a higher resolution of the high-intensity region

of interest.

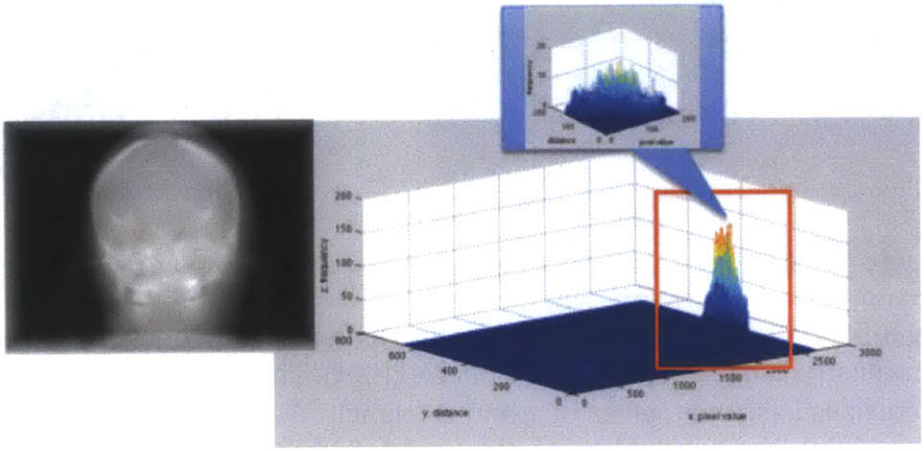

Figure 3-6: Full shape distribution *S(I)* (bottom right) of image *I* (left), and reduction to only high intensity pixels for the creation of the shape distribution (top).

The shape distributions were normalized to 1 to provide invariance to the scale. It is necessary to establish correspondences between different shape distributions in order to compensate for the anisotropic scales. Then the algorithm prepared the collection of the shape distributions characterizing a variable space of small-scale transformations of the patient volume image, which is referred to as the sparse base transformation set.

3.5 Objective Function

Once we computed the shape distributions for two image modalities, we evaluated the objective function as the similarity between the shape distributions of the input 2D projection images *SU(i)* and the 3D reference volume *SV(j)*. The similarity between the shape distributions of the images and the volume is evaluated by a cross-correlation function *C* that measures the change between two variables. The correlation coefficients in

C are the quantities that give the quality of a least squares fit to the original data and show the strength of a fit by the magnitude of the linear relation.

In the optimization step, the objective function is typically evaluated over the defined domain to identify the extrema. In this case, *C* is the correlation coefficient matrix of the shape distributions between input images and the base volume defined the objective function.

By considering two series of shape distribution variables *SU(i)* and *SV(j)* where *j=0,1,2...N-1*. The cross-correlation matrix *C* is defined in Eq. 3.3 as [33]:

$$C_{i,j}(SU,SV) = \frac{\sum_i (SU(i) - \overline{SU})(SV(j) - \overline{SV}]}{\sqrt{\sum_i (SU(i) - \overline{SU})^2}\sqrt{\sum_i (SV(j) - \overline{SV})^2}} \tag{3.3}$$

In *C* we have the cross-correlation coefficients *r*, which gives the goodness of the fit for the best possible linear function describing the relation between *SU* and *SV*. The coefficients *r* lies on the range [-1,+1] and is defined as the covariance of the two variables divided by the product of their standard deviations. A value of $r = 0$ means there is no correlation between *U* and *V*.

A value of 1 implies that a linear equation describes the relationship between *X* and *Y* perfectly, with all data points lying on a line for which *Y* increases as *X* increases. A value of −1 implies that all data points lie on a line for which *Y* decreases as *X* increases. The correlation coefficients are invariant to separate changes in location and scale of the two shape distribution sets.

Cross-correlation is efficiently used to define the objective function whereby the input transformation T is subject to an unknown combination of 6-DoF combinations, as shown below in Eq. 3.4 [34]:

$$T = \sum c_1(dx = 1, 2, \ldots) + \sum c_2(dy = 1, 2, \ldots) + \sum c_3(dz = 1, 2, \ldots) + \sum c_4(\theta x = 1, 2, \ldots) + \sum c_5(\theta y = 1, 2, \ldots) + \sum c_6(\theta z = 1, 2, \ldots) \quad (3.4)$$

Coefficients c_n for n = [1,6] is determined for each base function defined in the sparse base set for 6 DoF. We define a sparse base function set that is comprised of a small set of shape distributions of the volume perturbed by a set of single DoF transformations that span the 6-DoF small-scale transformation space.

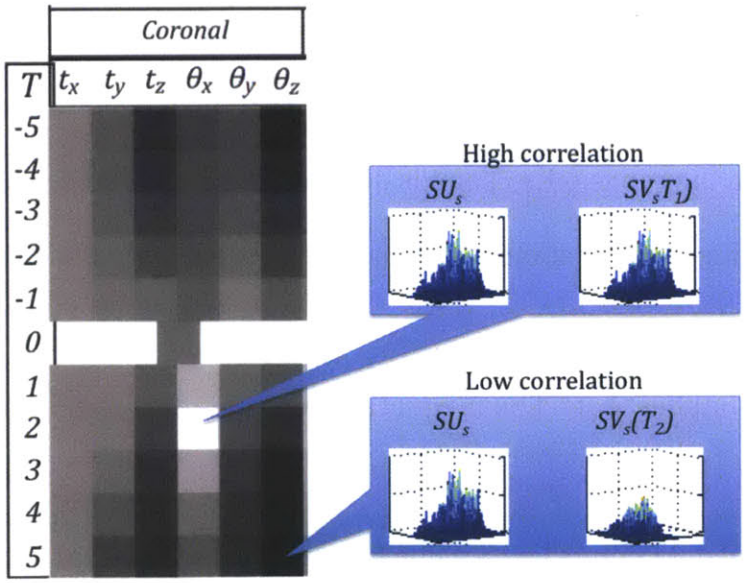

Figure 3-7: Correlation coefficients *C(SU,SV)* between the shape distribution *SU* of input image in relation to a set of 61 base functions.

The objective function provides correlation coefficients *C(SU,SV)* between the shape distributions of the orthogonal pair of images U_n that have undergone an unknown transformation *T* and the sparse base set of orthogonal projections volume *V*. By comparing the shape distributions between the base and input images, *C(SU,SV)* provides correlation information between the input and base images from which the discrete 6-DoF transformation values maybe extracted.

We ensure that the correlations are statistically significant by evaluating the p-values, *P(SU,SV)*. The p-values *p(i,j)* are computed by transforming the correlation to create a t-statistic having *n-2* DoF, where *n* is the number of rows of *X*. *P*, a matrix of p-values for testing the hypothesis of no correlation. Each p-value is the probability of getting a correlation as large as the observed value by random chance, when the true correlation is zero. If *p(i,j)* are sufficiently small, then the correlation *r(i,j)* is statistically significant. Base functions only with statistically significant p-values are considered in optimization.

3.6 Optimization

Lastly, the optimization step analyzes the correlation coefficients provided by the objective function and provides the best fitting 6-DoF transformation that maps *U* to *V*. Optimization identifies the most probable transformation *T* with a multi-step approach.

The first step in optimization is to decompose *C* into two types of transformations: translations and rotations. The translations and rotations are treated separately to distinguish the impact of the transformation the data set: rotations impact the placement of all pixels in all three dimensions, whereas translations affect the position of pixels in only one dimension.

The second step of optimization is to determine a correlation coefficient threshold that demarcates a high probability of an accurate match. This value was determined empirically because the interpretation of the correlation coefficient is dependent on the context and purpose of the application, e.g. the specific image registration setup and type of image modalities used.

We devised various cases defined by geometric constraints of 6-DoF transformations that can be used to optimize C with best fit. For example, a translation in the x–y plane will not affect the orientation in the z-plane so correlations related to this translation will only be apparent from the view of the x-y plane.

Additional constraints to the optimization algorithm were derived from the gradient ascent and descent recognition of C along each DoF. For example, the correlation between U and V that suggests $tx = 3$ will be shown in C with a maximum correlation at $tx = 3$ and a gradual ascent towards this value on the range of $tx = [-5,5]$.

In C we have cross-correlation coefficients r that give us the goodness of the fit for the best possible linear function describing the relation between SU and SV.

The optimization step provides that most statistically likely 6-DoF transformation that optimally aligns U to V with the use of various approaches and constraints imposed on C.

3.7 Accuracy

We measured the registration results as each individual translation and rotation obtained from the registration algorithm in comparison with the original transformation for transformation set and calculated targeting error ΔD. The total targeting error was expressed as:

$$\Delta D = \sqrt{(\Delta x + zt \cdot \Delta\theta y - yt \cdot \Delta\theta z)^2 + (\Delta y + xt \cdot \Delta\theta z - zt \cdot \Delta\theta x)^2 + (\Delta z + yt \cdot \Delta\theta x - xt \cdot \Delta\theta y)^2} \quad (3.5)$$

where the position coordinates of the target are *(xt,yt,zt)* and the error in the transformations are *(Δx, Δy, Δz, Δθx, Δθy, Δθz)* [35]. The targeting error metric *ΔD* was used to measure the accuracy of the alignment between the actual and calculated transformation between *U* and *V*.

3.8 Sensitivity

In order to test the robustness of the image registration algorithm, we introduced shot noise to both input images *U*.

Artificial shot noise was introduced to our datasets because this shot noise is dominant when a finite number of particles that carry energy are sufficiently small so that uncertainties due to the Poisson distribution are significant. Shot noise is a realistic factor that affects the quality of our images because the variations of current in the x-ray detector and DRR generation may cause the occurrence of independent random events that are significant enough to affect the intensities of the image pixels. The parameters of the Poisson noise were dependent on the input pixel values, which added Poisson noise to the image by calculating the means of Poisson distributions.

3.9 Summary

The algorithm first pre-processes the 2D input image data *U* and 3D base image data *V* to contain homologous intensities and crops the images to discard extraneous information in the image. Then for each input and base image representing the position of an image, the shape distribution objective function *F(I)* creates a characteristic distribution

of each image I which contains characteristics of its transformation. Then the objective function, a correlation function enumerates the correlation between shape distributions of the input images SU and the base volume SV. The correlation coefficient matrices C identify the transformations that most similarly match the SU and SV. The optimization method spans the objective function and quickly identifies the transformations of highest statistical likelihood that align the orthogonal projection images U to the base volume set V and provides the necessary relative 6-DoF patient positioning transformation during optimization.

4. Results

The results from the 2D-3D image registration algorithm are presented in this chapter. Chapter 4 introduces the experimental framework used to characterize the performance of the shape distribution registration algorithm. The details of our method used in a sequence of test experiments used to verify the validity of this algorithm are described. The 2D and 3D image datasets used in the results are identified. We present results of speed, accuracy, and sensitivity from the 2D-3D image registration algorithm with DRR-DRR data.

4.1 DRR-DRR Image Registration Outline

The shape distribution algorithm was used first to register input images U composed of the coronal and sagittal projection images (U_c, U_s, respectively) generated from the DRR, and the pair of projection images from the 3D base volume set V generated by the DRR. The DRR is derived from CT-simulated images of a phantom head. The image registration process can be simplified into four main steps:

1) preprocessing of the input images and the volume base set,

2) developing the characteristic shape distributions,

3) optimizing the objective function defined by the shape distributions with correlation, and

4) identifying the most optimal 6-DoF transformation.

The DRR-DRR image registration simulates stereotactic radiotherapy treatment: the 3D DRR image is provided by treatment planning when the patient's tumor is analyzed and quantified, and the pair of orthogonal 2D images are provided when the patient is placed in the radiation treatment room preparing for radiation therapy.

We sampled 6-DoF transformations categorized in four categories:

1) *Cat1:* transformations composed of only translations of the range [-5,5] pixels with increments of 1 pixel,

2) *Cat2:* transformations composed of only rotations of the range [-5,5] degrees with increments of 1 degree,

3) *Cat3:* combination transformations composed of translations of the range [-5,5] pixels of increments of 1 pixel and rotations of the range [-5,5] degrees with increments of 1 degree, and

4) *Cat4:* a set of unique 6-DoF transformations that include sub-pixel adjustments within or outside of the domain of the sparse base volume set.

There were 1331 samples in *Cat1,* 1331 samples in *Cat2*, 15,625 samples in *Cat3*, and 50 samples for *Cat4.*

4.2 Data Preprocessing and Initialization

The data preprocessing steps outlined in Chapter 3 guided the primary registration of the 2D and 3D images. This step smoothed the intensity values in the images to reduce the noise. Then we reduced the domain of the image by cropping out the background the images and kept the full skull surrounding the brain intact to reduce computational requirements necessary for alignment.

In the cases of DRR-DRR registration, the intensities of the data sets were not adjusted since both the 2D and 3D images are of the same modality and are already of isotropic scale.

The set of pairs of 2D-projections generated from volume set composed of 152-CT slices are of original resolution 1028x768. The 3D volume set of the phantom is generated from the DRRs. We create a sparse base transformation set by saving projection images of small-scale perturbations of the volume image. The elements of the base function set are individual 6-DoF transformations spanning the region of small-scale of perturbations as defined.

We defined the sparse base transformation set over a series of small-scale perturbations with N =5, as [-5,5] pixels of translation (over a range of 5.098 mm) in any one direction in increments of 1 pixel, or ±[-5,5] degrees in rotation about any axis with increments of 1 degree. Defining the sparse base transformation set over the range of 5.098 mm is a realistic expectation of the relative transformations since the objective of this algorithm aims to identify fine adjustments in patient positioning. The sparse base transformation sets of the coronal and sagittal projections of the base volume are shown in Appendix B. The sparse base transformation set is transformed as the volume base set under the T as defined in the structure below in Table 4-1. The notation of the 6-DoF transformations are written in shorthand as $(tx, ty, tz, \theta x, \theta y, \theta z)$ where tx, ty, and tz are units of pixels and θx, θy, θz are in degrees.

Table 4-1: A set of transformations *T* applied to base volume *V* to establish the sparse base transformation set spanning *N* units of perturbation.

(N,0,0,0,0,0)	*(0,N,0,0,0,0)*	*(0,0,N,0,0,0)*	...	...	*(0,0,0,0,0,N)*
(N-1,0,0,0,0,0)	...				
(N-2,0,0,0,0,0)		...			
...			...		
(0,0,0,0,0,0)					
...				...	
(-N+2,0,0,0,0,0)					
(-N+1,0,0,0,0,0)					
(-N,0,0,0,0,0)	*(0,-N,0,0,0,0)*	*(0,0,-N,0,0,0)*	*(0,0,0,N,-0,0)*	*(0,0,0,0,-N,0)*	*(0,0,0,0,0,-N)*

The data preprocessing steps defined the input and base image datasets to be in the same domain in terms of both image anatomical space and intensity. All images are filtered to reduce noise in the intensity of the images.

The isocenter of the input images was recorded as the geometric midpoint between the skull edges and the isocenter of the base volume was recorded as the geometric midpoint between the skull images of the baseline transformation.

4.3 Shape Distribution

The shape distributions are developed for each image *I* within the coronal and saggital projection image sets of *U* and *V*. The shape function *F(I)* samples each pixel in the domain space as its intensity and distance from the isocenter. The shape distribution samples the full domain of the image following the anatomical reduction of the image. Pixels of intensities significantly higher than that of air, e.g. bone and metal implants, are

saved to reduce computational requirements; pixels of intensities comparable to air are discarded.

The shape distributions were binned a distance range of 200 pixels and an intensity range of about 250 to further compress the size of the shape distribution. The shape distribution of the orthogonal projections shown in Fig. 4-1 is of the coronal projection, and the shape distribution of the sagittal projection is shown below in Fig. 4-2.

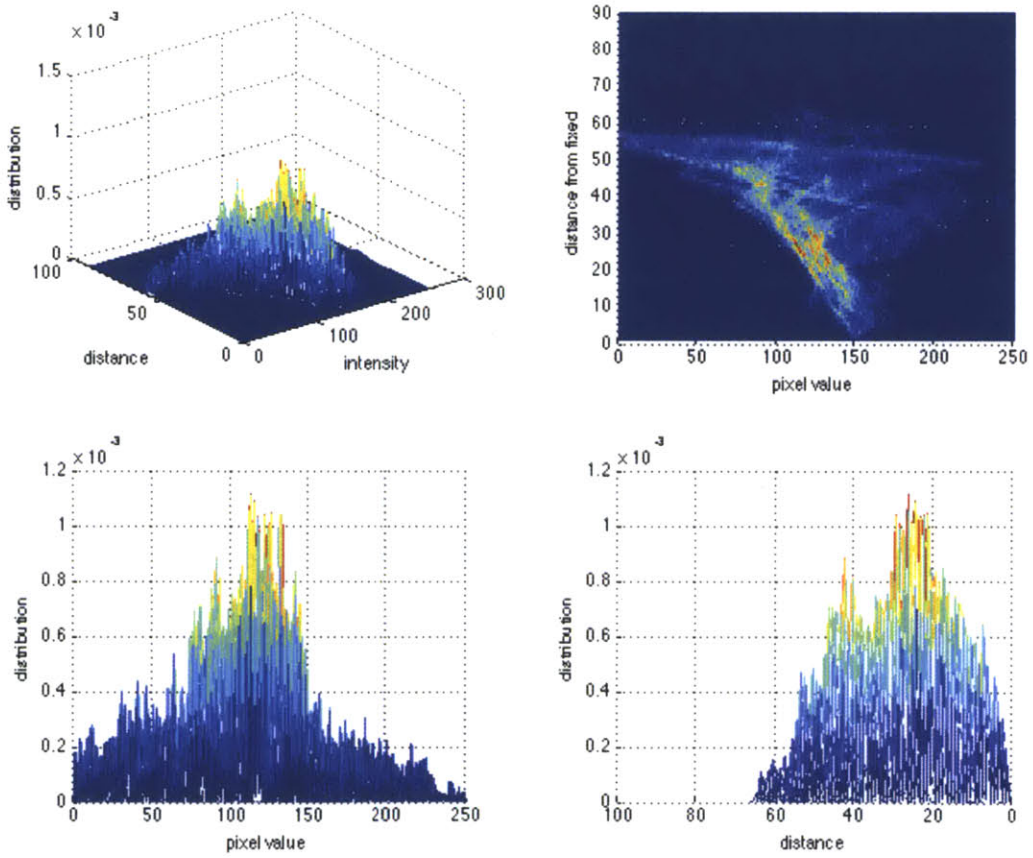

Figure 4-1: Shape distribution of 2D coronal projection U_c transformed by T = (0,0,0,0,0,0): 3D shape distribution (top left), pixel vs distance (top right), pixel vs distribution (bottom left), distance vs distribution (bottom right).

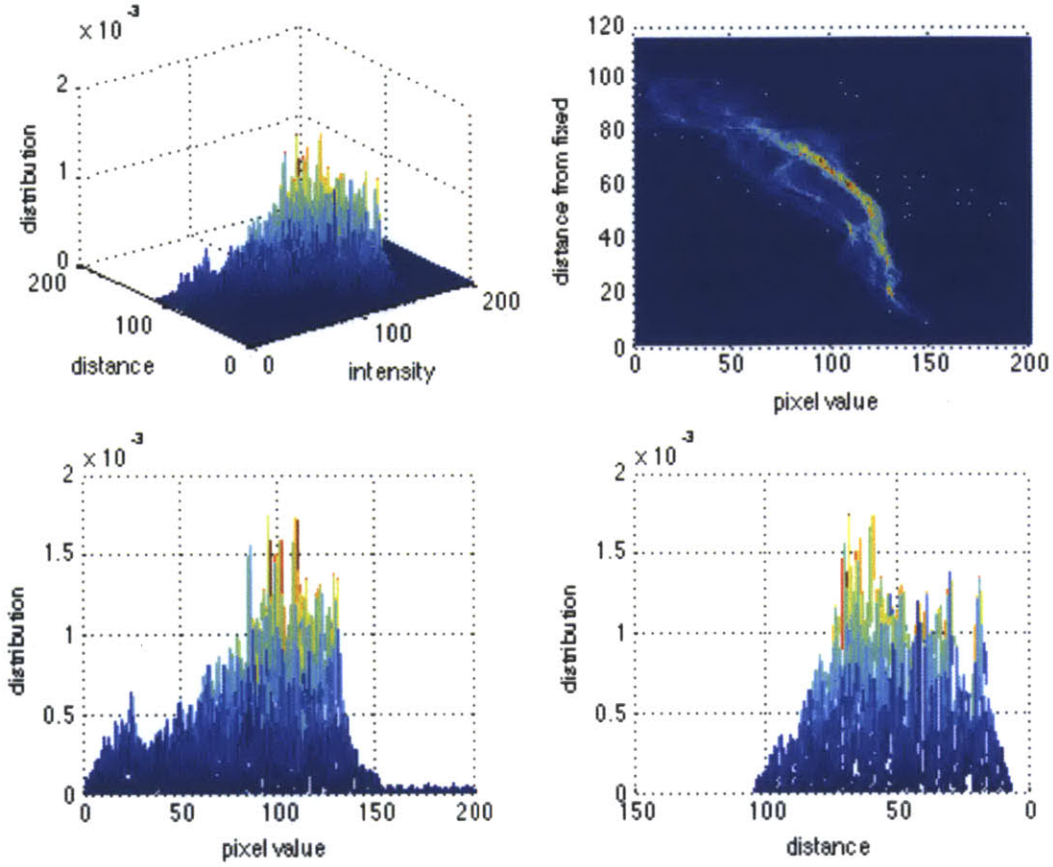

Figure 4-2: Shape distribution of 2D sagittal projection U_s transformed by T = (0,0,0,0,0,0): 3D shape distribution (top left), pixel vs distance (top right), pixel vs distribution (bottom left), distance vs distribution (bottom right).

By sampling the full sparse base transformation space defined previously in the preprocessing step in Table 4-1, a sparse base function set is populated. For each independent transformation of the volume in the base transformation set, a characteristic shape distribution is developed. The shape distributions for each respective transformation of the volume are shown in the Appendix in the same layout defined in Table 4-1.

Once shape distributions of both the input images and transformations of the base images were created, the shape distributions were evaluated in the objective function.

4.4 Objective Function

The shape distributions from the 2D projection images were correlated against the sparse base function set containing the shape distributions developed from the 3D volume set. *C(SU,SV)* shows the correlation of each pixel in the shape distribution of the input image series *SU* against the respective pixel in the shape distributions of that transformation in the shape distribution base set *SV*. Each row of Fig. 4-3a (left) represents the correlation of the input image of the shape distribution of each transformation against that of each DoF of the volume base set. Fig. 4-3b (right) represents the correlation matrix for the input image compared against the volume base set for the sagittal view.

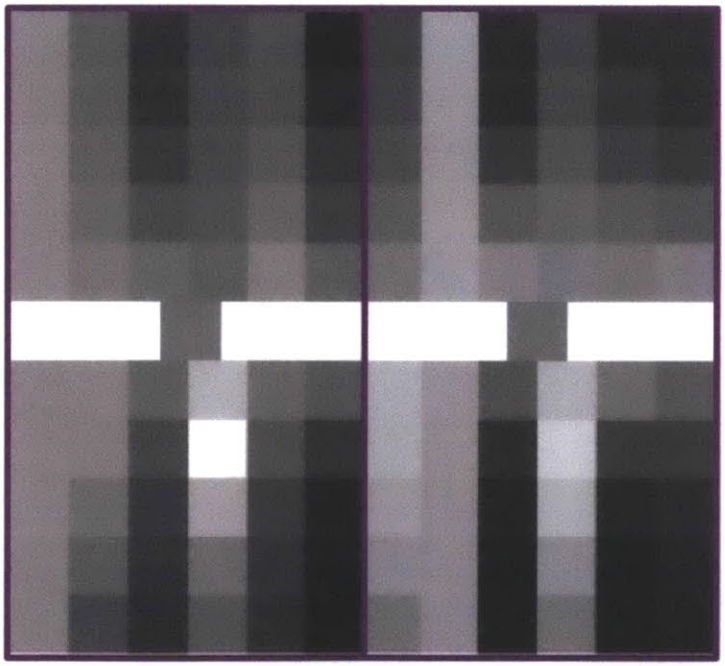

Figure 4-3: Correlation matrix C_c of the shape distribution correlations between the input coronal view and the base volume coronal views (left), and correlation matrix C_s of the shape distribution correlations between the input sagittal view and the base volume sagittal views (right).

The correlation matrices $C_c = C(SU_c,SU_c)$ and $C_s = C(SU_s,SU_s)$ establish the domain of the objective function from which the optimization function evaluates. The pair of correlation matrices C in Fig. 4-3a and Fig. 4-3b are evaluated to identify the 6-DoF transformation that maximizes the alignment between the 2D orthogonal input images and the 3D volume set. The correlation values between 2D and 3D images that surpass a minimum threshold signify a sufficiently high correlation between the alignments of the images. The correlations of some 6-DoF transformations that map the 2D to 3D images are visible in the coronal view but not in the sagittal view, and vice versa due to the effect of the transformation on the projection. This logic guides the interpretation of the correlation matrices to determine the optimal positioning. Fig. 4-4 depicts the elements of highest correlation between the shape distributions of input set U and base set V.

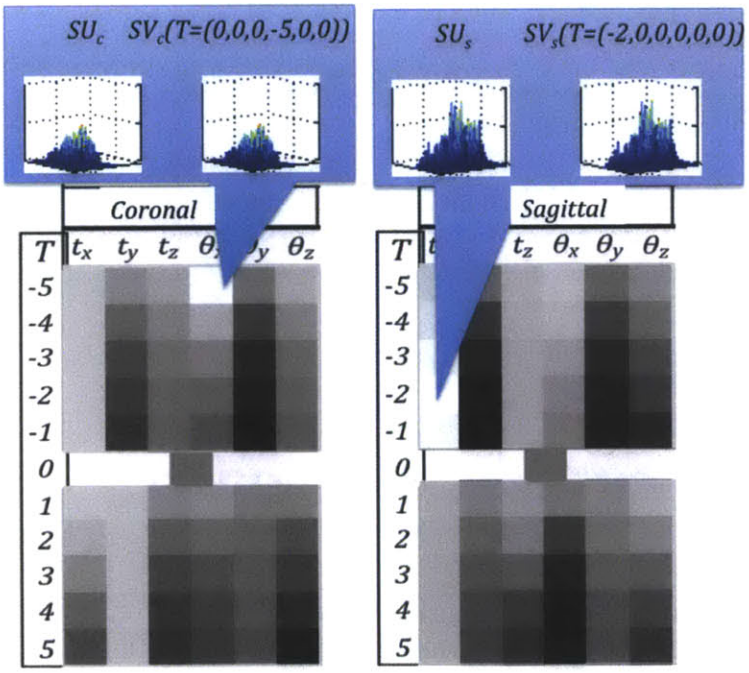

Figure 4-4: Correlation matrices. SU_c correlates highest with $SV_c(T = (0,0,0,-5,0,0))$. U_s correlates highest with $V_s(T= (-2,0,0,0,0,0))$.

The correlation coefficients r gives a high goodness of fit for T_{tot} describing the relation between U and V. The correlation coefficients threshold was set to 0.15 with respect to the specific data presented.

The p-values of the correlation coefficients were then evaluated to identify whether or not the correlations above were statistically significant transformations.

We evaluated the p-values, p, the probability that a variate would assume a value greater than or equal to the observed value strictly by chance, of the automatically registered 6 DoF to ensure that the correlations are statistically significant as $p = P(z \geq z_{observed})$. The significance level z was set to 0.001 such that if the sample results are less than or equal to that, the match of (i,j) is statistically significant. The algorithm picks the most likely 6-DoF transformation only if the solutions with p-values are significant.

4.5 Optimization of the Objective Function

The objective function defined above is optimized to determine the transformation that maximizes the alignment between the 2D orthogonal input images and the 3D volume set for each transformation. The optimization step provided the 6-DoF transformation as a linear combination of elements of the sparse base transformation set as the highest statistical match mapping U to V.

4.6 Speed Criterion

In Matlab, the offline steps of data preprocessing and development of the 3D volume for the sparse base transformation set with a range of [-5,5] pixels and [-5,5] degrees were

calculated in an average of 3.251 minutes.[f] The offline steps begin with one 3D model and output a pair of shape distribution sets, one for the coronal projection images and one for the sagittal projection images.

The speed of each step in the algorithm as measured by various cases of transformation T is listed below in Table 4-2.

Table 4-2: Speed of each online process in the image registration algorithm.

	Preprocessing U (s)	SU_c (s)	SU_s (s)	C_c (s)	C_s (s)	Optimization (s)
Average	0.1953	0.0155	0.0187	0.0713	0.0736	0.1532
Standard Deviation	0.0702	0.0010	0.0013	0.0188	0.0179	0.0096
Minimum	0.1104	0.0131	0.0155	0.0619	0.0643	0.1354
Maximum	0.3325	0.0165	0.0202	0.1272	0.1261	0.1654

The average speeds of each process were: 0.1953 s for data preprocessing, 0.0155 s for creating the shape distribution for the coronal projection, 0.0187 s for making the shape distribution for the sagittal projection, 0.0713 s for correlating the coronal view against the base set, 0.0736 s for correlating the sagittal view against the base set. The total offline calculation speed requires 185.06 s, and the average total online calculation requires 0.5276 s.

4.7 Accuracy

We measured the registration results as each individual translation and rotation obtained from the registration algorithm in comparison with the original transformation

[f] It is important to note that both the data preprocessing step and the generation of the sparse base transformation can be computed offline before the patient enters the treatment room, so this does not compromise the time it takes for patient positioning in the treatment room.

for transformation set and calculated targeting error ΔD. The errors of three translations and three rotations between the original transformation and the transformation determined by the algorithm are described by the target position coordinates (xt, yt, zt) and the error in the transformations $(\Delta x, \Delta y, \Delta z, \Delta\theta x, \Delta\theta y, \Delta\theta z)$. The total targeting error was expressed in Eq. 3.5.

Table 4-3: Evaluation of image registration algorithm in terms of targeting error ΔD. *Cat1* is the set of translational transformations, *Cat2* is the set of rotational transformations, *Cat3* is the set of combination transformations, and *Cat4* is a unique series of transformations defined in Ch. 4.1.

	ΔD of *Cat1*	ΔD of *Cat2*	ΔD of *Cat3*	ΔD of *Cat4*
Average	0.693	0.813	0.216	0.635
Standard Deviation	0.237	0.235	1.033	0.423
Minimum	0.000	0.000	0.000	0.000
Maximum	6.929	5.237	4.334	3.132

The targeting error ΔD of a sparse sampling of *Cat1* is shown below in Fig. 4-6. The area of the marker is directly proportional to the cube of the targeting error magnitude. The three axes are the three individual translational DoFs, (*tx,ty,tz)*.

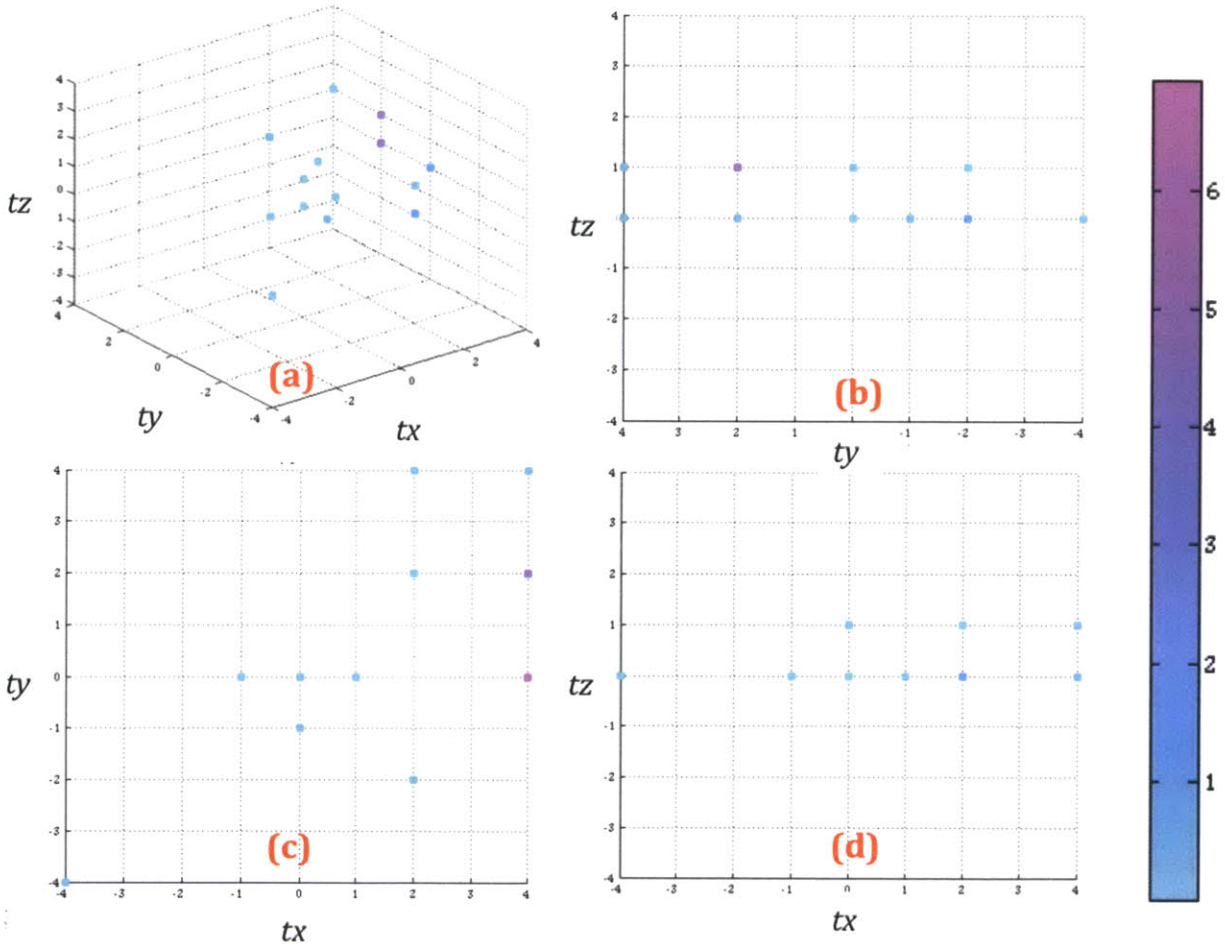

Figure 4-5: Targeting error ΔD of a sparse sampling of *Cat1*. The perturbations *(tx, ty, tz)* are plotted on their respective axes and the magnitude of ΔD is represented by the color (a). The *ty-tz* projection is shown in (b), *tx-ty* is shown in (c), and *tx-tz* is shown in (d).

Similarly, the targeting error ΔD of a sparse sampling of *Cat2* is shown below in Fig. 4-7. The area of the marker is directly proportional to the cube of the targeting error magnitude. The three axes are the three individual rotational DoFs, (θx, θy, θz).

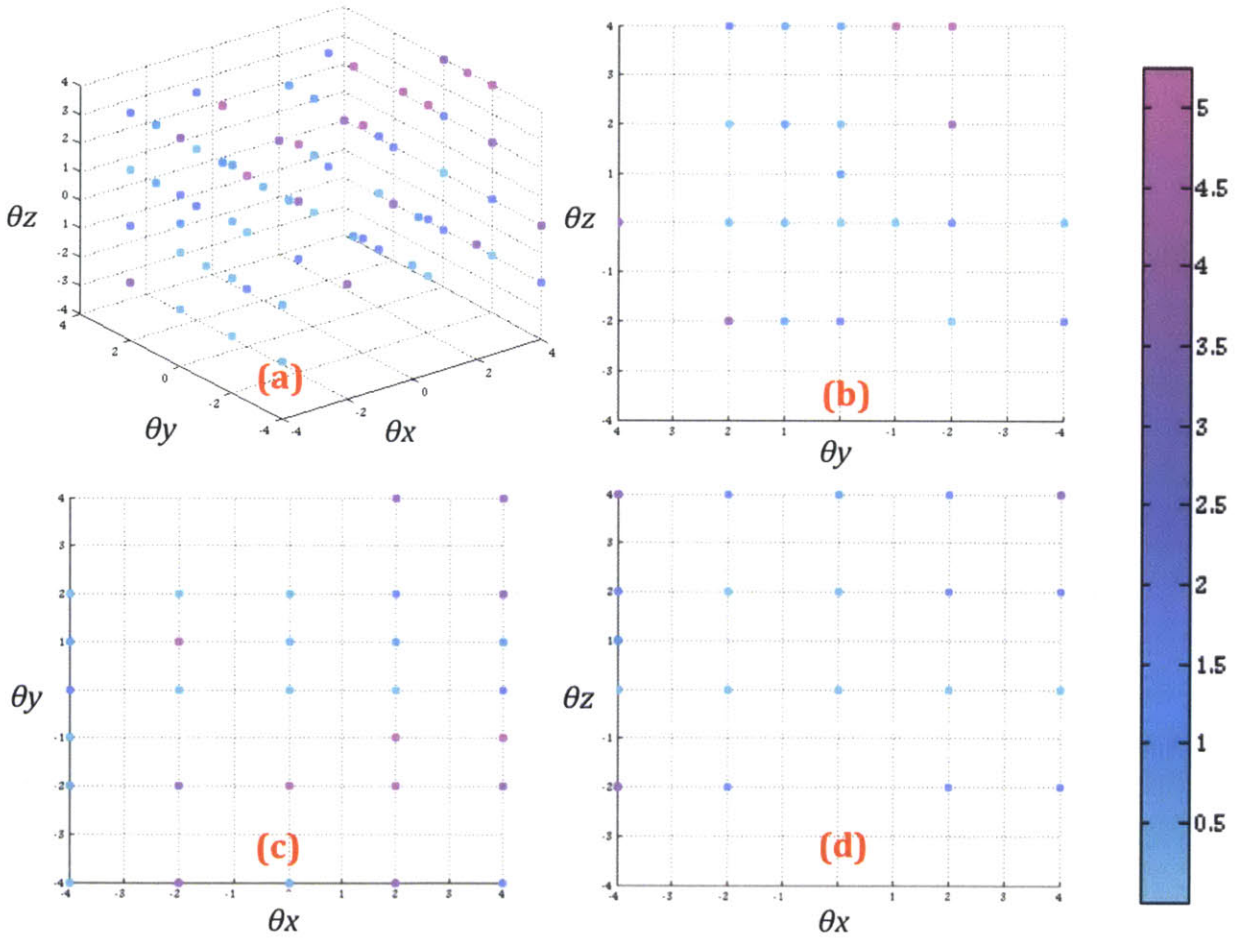

Figure 4-6: Targeting error ΔD of a sparse sampling of *Cat2*. The perturbations (θx, θy, θz) are plotted on their respective axes and the magnitude of ΔD is represented by the color (a). The θy-θz projection is shown in (b), θx-θy is shown in (c), and θx-θz is shown in (d).

We enumerate the registration errors of transformations T of all sets defined in

Cat1, *Cat2*, and *Cat3* by the DoF of the error in Table 4-4. The following table contains the errors of translations and rotations between the registration method estimations and the real transformations.

Table 4-4: Registration errors of translations, rotations, and both, of the set of all T transformations defined in *Cat1*, *Cat2*, and *Cat3*.

	Errors of translations (pixel)			Errors in rotations (degree)			
	tx	*ty*	*tz*	*θx*	*θy*	*θz*	*Overall*
Average	0.5556	0.5556	0.2222	0.0347	0.2932	0.8906	0.4253
Standard Deviation	0.2326	0.2154	0.4237	0.3203	0.2273	0.2096	0.2715
Minimum	-4	-4	0	-4	-4	-4	-3.333
Maximum	4	4	1	4	4	4	3.000

4.8 Sensitivity

In order to test the robustness of the algorithm, we introduced shot noise to modify pixel intensities in the images U by adding Poisson noise directly to the image as a modification of pixel intensities.

Then, the optimization method selected the most optimal 6-DoF transformation of these elements in the sparse base function.

Table 4-5: Sensitivity evaluation of image registration algorithm in terms of targeting error with input images U treated with shot noise.

	ΔD of *Cat1*	ΔD of *Cat2*	ΔD of *Cat3*	ΔD of *Cat4*
Average	0.693	0.813	0.216	0.635
Standard Deviation	0.237	0.235	1.033	0.423
Minimum	0.000	0.000	0.000	0.000
Maximum	11.021	2.237	4.334	3.132

The addition of shot noise to U did not change the targeting error of the algorithm image registration estimations.

5. Discussion

The shape distribution image registration algorithm is fast, efficient, and accurate at providing a predictive 6-DoF transformation mapping U to V by creating shape distributions characteristic of transformed images, and then correlating them against a sparse base transformation set. This method does not directly depend on feature-, or intensity- based homologous points, an aspect of current image registration methods that commonly triggers registration errors. The algorithm is able to automatically register 2D-3D DRR images accurately and quickly.

The image registration algorithm generally had sub-pixel accuracy in finding 6-DoF transformations as linear combinations of independent single-DoF transformations in DRR-DRR image registration by correlating their shape distributions against the sparse base transformation set.

5.1 Speed Criterion

The algorithm affords fast offline calculations of the sparse base set on the treatment planning data, as well as fast online calculations on the input data from a pair of real-time 2D images.

In Matlab, the offline steps of data preprocessing and development of the 3D volume for the sparse base transformation set with $N = 5$ was calculated in an average of 3.251 minutes. The offline steps begin given one 3D volume model of the patient, and then calculate and output a pair of shape distribution sets, one for the coronal projection images

and one for the sagittal projection images. The data preprocessing step and the generation of the sparse base transformation can be computed in the computer system without requiring use of the radiation treatment facilities, shortening treatment planning time and increasing treatment room capacity.

For the online calculations, the average speed of each step was: 0.1953 s for data preprocessing, 0.0155 s for creating the shape distribution for the coronal projection, 0.0187 s for making the shape distribution for the sagittal projection, 0.0713 s for correlating the coronal view against the base set, 0.0736 s for correlating the sagittal view against the base set. The longest online step was preprocessing of the data. The standard deviations were under 0.02 s for each of the online steps.

The total offline calculation speed requires 185.06 s, and the average total online calculation requires 0.5276 s. It is important to note that the evaluation of the speed was dependent on a computer clock, so these speed values may reflect uncertainties in timing by the automated clock.

5.2 Accuracy

The base transformation set is composed of shape distributions distinct to 1 pixel. By comparing the original transformations of the 2D images with the transformation selected by the registration algorithm, we can conclude that the selection of the 6-DoF transformation is accurate to at least one pixel.

The accuracy of the image registration algorithm as evaluated by the targeting error was with sub-pixel accuracy for all categories evaluated in the results. Most standard

deviations of targeting error maintained sub-pixel accuracy of the patient positioning transformation estimation.

A caveat to the output of the automatic image registration method is that at small-scale perturbations, more than one combination of transformations can lead to similar solutions of the objective function. In this image registration algorithm, two different 6-DoF transformations may orient U to V with different pose estimations. The emergence of the differing pose estimations is due to degeneracy. Degeneracy is the solution set is the limiting case in which a class of transformations changes to belong to another class as a result of similar evaluation of the objective function. Cross-correlation matrices C define the domain of the objective function, which the optimization method evaluates to identify the most statistically likely transformation. While a pair of cross-correlation matrices presents bi-planar information about the pose of the 3D object, more information must be provided about the generation of the transform to produce a complete set of non-degenerate solutions.

Effectively, degeneracy increases the magnitude of the targeting error metric and implies a reduction of the accuracy of the algorithm.

We have defined the solution space to have 6 DoF to describe the transformation T with six distinct parameters. T has been defined as an affine, rigid-body transformation that can map the 3D volume base set as a set of three non-degenerate points to three non-degenerate points given bi-planar images. The algorithm shows degenerate solutions by estimating the transformations to the most statistically relevant series of independent transformations, which are commonly lost at the range of small perturbations.

Degeneracy of this algorithm in the sparse model occurs as the reduction of more complex input transformations to reduced 6-DoF *T* approximations with high accuracy. The mathematically distinct range of solutions developed by the sparse base set establishes the domain from which the 6-DoF transformation *T* estimation can be composed. At small-scale perturbations, transformation estimations resulting from the optimization of the objective function may produce similar cross-correlation values that are interpreted to lead to degenerate solutions of the objective function. Because the current optimization method is driven by statistical values of correlation between the input images and the base images, the algorithm is susceptible to degeneracy.

Overall, the image registration method has sub-pixel accuracy with registering DRR-DRR images. A closer examination of Table 4-4 views all transformations defined in *Cat1, Cat2, and Cat3,* and then shows errors categorized by each DoF. The discrepancies in magnitude of targeting error by each DoF may be due to the original image quality and the shape distribution characterization of the images.

Targeting error is an effective metric at evaluating the magnitude of distance from the targeted set of points given the error in each DoF. Targeting errors in *tx* and *ty* show similar errors in terms of average, standard deviation, and range. This result meets expectations since the images are of the same resolution in x and y. Targeting error of *tz* is lower than of *tx* and of *ty.* This difference may be explained by the resolution of the image along the z-direction. I hypothesize that because the pixel spacing is much larger along the z-axis than along the x- or y-axis, the shape distributions are more distinctive, leading to a lower average error in *tz.* However, because the spacing between each distinctive scan is

larger, the standard deviation in error of *tz* may larger as a result of the interpolated intensities.

Similarly, the differing resolution of the DRRs in the z-axis may have caused the mean error in θ_z to be higher than those of θ_x and θ_y. It is hypothesized that θ_x is more accurate than the other two rotational DoFs because of the distinctive shape distribution transformation space of the sagittal projection.

5.3 Translational Transformations

Transformations composed only of translations as defined in a 6-DoF transformation space, *Cat1,* express high unitary correlations corresponding to matches shown in the correlation matrices C_c or C_s between the shape distributions of input and base images. The transformation correlation is shown as an element of high r either in C_c or C_s depending on the dimension of the translation. The translation will typically only affect one plane as a result of geometric description, since an entire plane will translate along an axis without affecting the position of the other two planes. This geometrical observation confirmed transformations as translations by showing high coefficients with significant p-values in one C but not the other.

The transformations in *Cat1* are accurate to an average of 0.693 pixels with a standard deviation of 0.237. *Cat1* has the largest maximum targeting error among the four categories at 6.929 pixels.

Degeneracy poses an issue in transformation estimations amongst *Cat1*. To give an example of degeneracy, input transformation T = (2,4,4,0,0,0) mapping between U and V is estimated by the algorithm to be mapped by a transformation T = (1,0,3,0,0,0); targeting error is 4.5826 pixels.

5.4 Rotational Transformations

Transformations composed only of rotations in a 6-DoF system express match correlations to the rotation elements in the base transformation set, as shown in C_c or C_s. The correlations in both C_c and C_s are affected by the rotations because geometrically, rotations affect the orientation of the 3D object in all three planes. The results are relatively high correlations shown in both C_c and C_s due to the geometrical effect of T in all three dimensions.

The transformations in *Cat2* have sub-pixel accuracy, with an average of 0.813 degrees, and a standard deviation of 0.235 degrees. An example of a degenerate case in *Cat2* is a real transformation on U of T = (0,0,0,2,4,4) that is estimated by the algorithm to be T = (0,0,0,0,5,0). The targeting error of this example is ΔD = 5, whereas the actual transformation between U and V may still abide to higher accuracy.

5.5 Combination Translation/Rotation Transformations

The combination of both translation and rotation transformations induces overall lower correlations shown in C_c and C_s due to the geometrical effect of T of all three dimensions. In the optimization algorithm, it was possible to deduct combination transformations by combining the logic described above in Ch. 5.2 and Ch. 5.3. However due to the nature of multiple transformations, the algorithm may have provided many degenerate solutions of the 6-DoF transformation.

We see that the targeting error for *Cat3* is on average 0.216 pixels, the smallest average among all categories. However, the standard deviation is 1.033, providing near-

pixel accuracy. The results of *Cat3* support further investigation for optimal deduction of transformation *T*.

5.6 Transformations outside of Base Set

There were several unique cases we tested in image registration matching in *Cat4* where the transformations could be interpolated or extrapolated from the base set, as they were of sub-pixel transformations or outside of the sparse volume base set. The algorithm was able to determine interpolated or extrapolated transformations in the optimization step due to the progression of statistically significant correlation coefficients against *U* and *V*. These cases show that the algorithm is able to process sufficient data to determine interpolation and extrapolation transformations.

For example, in the case where the input images were transformed outside of the sparse base transformation set, the algorithm shows potential for transformation extrapolation. In the case of $T = (0,0,3.5,0,0,0)$ where the input images were transformed by a unit undefined in the sparse base set, the algorithm shows the ability to interpret transformation interpolation. This was achieved by developing criterion in the optimization algorithm that identifies characteristic changes in correlation matrices *C* that distinguish interpolated *T*. These observations lead us to believe that there can be sub-pixel accuracy more refined than initialized by the domain of *V*.

5.7 Sensitivity

As shown by the sensitivity test of the introduction of shot noise to input images *U*, the algorithm is robust. The preprocessing steps smoothed the images and distributions. We did not find that the results of the algorithm were altered significantly by the artificially

added noise, as the algorithm was still able to interpret accurately the transformation between U and V as the same 6-DoF transformation. Therefore, we conclude that the algorithm is robust.

5.8 X-ray-DRR Image Registration

Registering x-ray to DRR images is a standard image registration process for stereotactic therapy. The same four-step image registration process as the DRR-DRR process above was applied to x-ray-DRRs:

1) preprocessing of the input x-ray images and the volume base set,

2) developing the characteristic shape distributions,

3) optimizing the objective function defined by the shape distributions, and

4) identifying the most optimal 6-DoF transformation.

As explained below, the adaptation of the current version of the algorithm as it is defined for DRR-DRR image registration was not easily extended to x-ray-DRR image registration.

The preprocessing step aimed to streamline the anisotropic range of the pixel intensities and generate the same pixel resolution between the two image datasets. It was not straightforward to define homologous anatomical regions such that both image modalities are of mutual domain.

One obvious difference between the two image modalities was the pixel resolution of the images. It was fairly straightforward to create replicate images of the same resolution while maintaining the geometric domain and pixel intensity values.

The use of poor x-ray and/or DRR images or varying levels of noise in the images may have caused registration difficulties.

A larger difficulty in extending this algorithm to work for x-ray-DRR image registration may have been due to the differences between the image qualities of the x-rays and the DRRs. Because DRRs are only approximations of and are not real x-ray images, the resulting DRR image may not be sufficiently similar for the development of an objective function by cross-correlation.

The generation processes of the images differ significantly whereby homologous points are represented by different numerical values. The ranges of pixel intensities are anisotropic, proving difficult to demarcate the high pixel intensity region that represents bone. The attenuation effects differ between the two image modalities and thereby change the image qualities, causing the inability to easily relate the pixel intensities with an automatic method.

The data preprocessing step posed an issue that was outside the realm of this thesis project, so instead of defining the objective function from this data, we investigated further the nature of relative transformations on the model given information of the model via the shape distribution characterization.

We were provided with x-ray images X and DRR images of volume V that imaged the same phantom. We were given three sets of x-ray images X: 1) *baseline*, 2) *shift 1*, and 3) *shift 2*. Both *shift 1* and *shift 2* underwent three translations, enumerated below in Table 5-1.

Table 5-1: Transformations of x-ray images *X*.

Transformation	Perturbation (mm)			Perturbation (DRR-pixel)		
	Longitude	*Latitude*	*Vertical*	*tx*	*ty*	*tz*
Baseline	0	0	0	0	0	0
Shift 1	1	2	3	-3.92	5.98	-1.96
Shift 2	-3	-2	-1	3.92	-1.96	5.98

To study the nature of the relative transformations, we transformed the two projections of *V* by the known transformations *shift 1* and *shift 2.* Pixel intensities of homologous points were manually aligned between *X* and *V*.

Intra-comparison of the shape distributions of the x-ray images *X* and of the DRR projection images of *V* shows that shape distributions provided distinctive characteristic information about the transformed images (see Fig. 5-1 and Fig. 5-2).

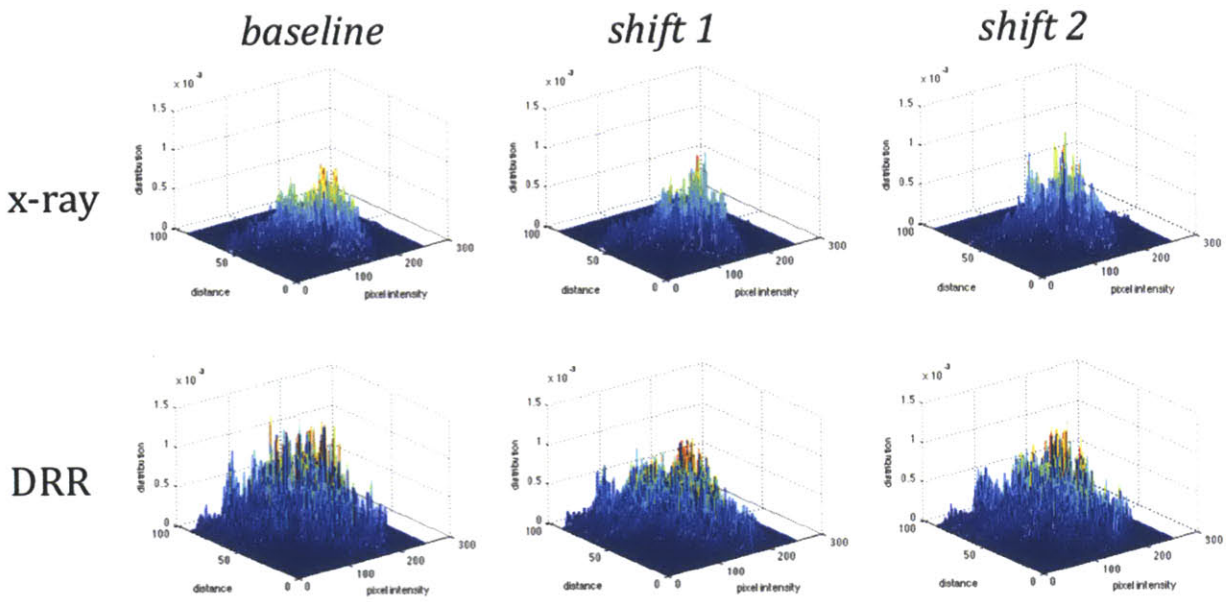

Figure 5-1: Shape distributions the coronal view of the phantom.

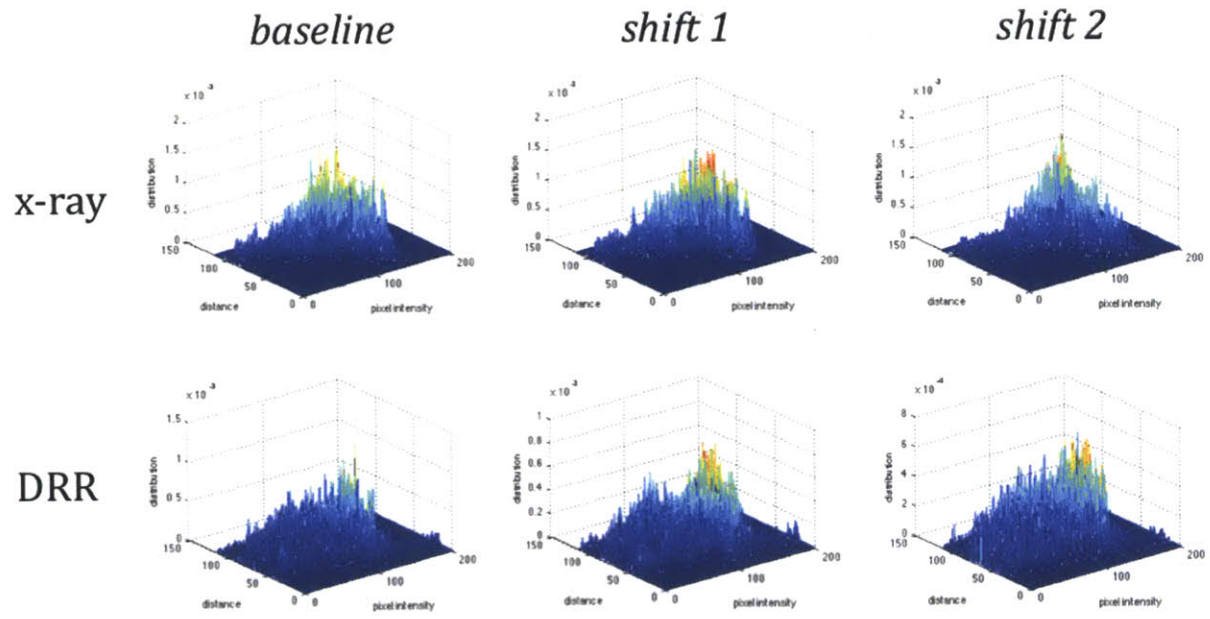

Figure 5-2: Shape distributions of the sagittal view of the phantom.

We have shown above that shape distributions are effective at representing images with characteristic descriptors. However in the current state of the art, we are limited by

the initial data processing of the x-ray and DRR image modalities to be able to determine relationships between the image modalities, limiting us from the definition of the objective function and the final determination of the relative transformation.

5.9 Summary

Overall, we found that this shape function tool is valuable for fast and accurate patient positioning in determining 6-DoF transformations from a sparse base transformation set. We have achieved the design constraints of accuracy, sensitivity, and speed necessary for this algorithm to be further researched for applicability in a clinical setting.

The complete algorithm was conducted in under four minutes, three minutes of which was in offline calculations. The online process to conduct a complete 2D-3D registration was well under a minute. The longest step in the online process was preprocessing the data.

The registration process was accurate to sub-pixel accuracy when the 6-DoF transformation was defined within the sparse base transformation set but was shown to be accurate to near-pixel accuracy when the 6-DoF transformation was interpolated or extrapolated from the base set.

The shape distribution algorithm is robust, due to the data-preprocessing step that removed noise and ensured that the intensity values and size of the domain were homologous. However, we found that the objective function defined by correlation was sensitive to outliers in the data. Statistical inference for the cross-correlation coefficient is sensitive to the data distribution.

This algorithm is especially useful for describing an image as a distribution of the selected characteristic shape attribute and thus, improves patient positioning time and accuracy while also reducing the radiation dose delivered to the patient during positioning.

6. Conclusion

We have introduced a novel algorithm for conducting 2D-3D image registration for stereotactic radiotherapy patient positioning. This thesis addresses the need for a fast and accurate patient positioning algorithm for stereotactic radiotherapy that would be easy to deploy, reduces radiation dose delivered to the patient, improves the accuracy of radiation dose delivery, increases comfort of the patient during the patient positioning process, and facilitates more efficient use of radiation treatment rooms. The main objective of our algorithm was to efficiently identify the accurate 6-DoF transformation that describe the optimal pose alignment between the pair of orthogonal 2D input images and the 3D base volume image set taken of the patient.

Our main contribution to the state of the art of patient positioning algorithms is the introduction of a sparse base set for prompt 2D-3D image registration. We first identified a number of issues associated with current image registration techniques and have focused on generating methods for addressing the central goals of accuracy, robustness, and speed. The algorithm allows for comparison of input 2D images against a 3D volume dataset with unknown pose, retrieves the complex transformation that maps the 2D set to the 3D set, and generates the most statistically likely 6-DoF transformation.

We designed an image descriptor, the shape distribution, to represent each image as a histogram of distances and pixel intensities to effectively characterize the pose of the patient image. The algorithm relies on the development of a set of shape distributions to

characterize each image uniquely.

We developed a mathematical model that was not based on prior clinical data and that does not anticipate an exact form of the input images. The algorithm requires the generation of a sparse base set of transformations of the volume that spans a small range of 6-DoF perturbations. An objective function is developed from the cross-correlation of the shape distributions of the input image against the sparse base transformation set which is then optimized to identify the most statistically likely 6-DoF transformation aligning the two datasets. We presented a framework for efficient registration of the 2D images to the 3D model with sub-pixel accuracy.

6.1 Experimental Results

We evaluated the registration algorithm with four categories of experimental results on DRR-DRR image registration. We showed that for DRR-DRR registration, the shape distribution algorithm robustly, quickly, and reliably determines the 6-DoF transformation that maps the 2D images to the 3D volume of the patient.

The first two experimental categories, the set only translational transformations and the set of only rotational transformations, within the base transformation set showed sub-pixel accuracy in determining the transformation. The combination transformations composed of both rotations and translations showed near-pixel accuracy.

The fourth category of experimental tests was composed of a unique set of transformations both outside of the base transformation set and of sub-pixel increments. The optimization method was able to deduce the transformations of these test transformations. The results have led us to believe that this algorithm has the potential to provide sub-pixel accuracy of transformations that is not reliant on the range of the base

transformation test and the domain of the objective function that develops from this base set.

The representation of the images by the shape distribution show that information about the pose of the 3D model provides sufficient information to provide sub-pixel accuracy of the alignment; thus, information about the pose is not lost in the shape distribution characterization.

The speed evaluation of the algorithm showed that the algorithm is able to conduct all offline calculations on average in 3.251 minutes and all online calculations can be conducted on average in 0.5276 s. The speed of the algorithm meets criterion to be sufficiently rapid for effective clinical application.

The sensitivity tests conducted by the introduction of shot noise to the input images ensured that the shape distribution image registration approach is robust. The estimated transformations were not effected by the noise.

Overall, this shape distribution image registration method has proven to be fast, accurate, robust, and does not suffer issues faced by current image registration methods, e.g. local extrema traps.

6.2 Future Research

We developed a framework for 2D-3D image registration with shape distributions. The concept of shape distributions is highly applicable beyond the scope of patient positioning for stereotactic radiation therapy on the brain given 2D input images and a 3D volume model. The following sub-sections of Ch. 6.2 describe techniques or concepts that could improve the current 2D-3D image registration algorithm or expand the applicable use of the concept of shape distributions for other complex imaging tasks.

6.2.1 Shape Functions

The algorithm in this thesis may be extended to explore the effectiveness of using additional or alternative shape functions to evaluate the domain space. Alternative shape functions can provide additional information that may have been lost with the characterization of images with the current shape function *F(I)*. We did not have the chance to examine other shape functions beyond the one we defined and tested. There is high potential of increasing robustness and accuracy of this algorithm by combining the use of several shape functions.

6.2.2 Additional Degrees-of-Freedom

This algorithm has the potential to identify more complex transformations with more degrees-of-freedom. The investigation of this algorithm on systems with more degrees-of-freedom may be geared for non-rigid bodies or for images that are skewed and stretched.

6.2.3 Additional Medical Applications

This algorithm proves the potential for the use for other medical image modalities. X-rays and DRRs are the most frequently used image modalities for stereotactic radiotherapy, so this algorithm can be further developed to serve as a method for registering x-ray and DRRs. In our initial investigation of x-ray-DRR image registration, the process of registering proved to be extremely difficult, possibly due to differences in the nature of differing pixel intensities.

There is room for future research in applying shape distributions to register other image modalities such as MRIs and ultrasounds. Additionally, the algorithm is not

restricted to the domain of the brain and further research may be conducted on the alignment of other body parts. Because there is no prior knowledge set built into this algorithm, the sparse base set can be variable depending on the input images.

6.2.4 Code Optimization

The current Matlab code has not been optimized for speed. It is possible to rewrite this current algorithm with more efficient methods and optimizing especially at calculation bottlenecks [36]. It would be of interest to compare our current algorithm with the algorithm after it is optimized with the fastest implementation techniques.

We found that the shape distributions worked best on our datasets when the number of bins of the shape distributions is set on the order of $1/200^{th}$ of the full pixel intensity range. We found that in general, increasing the bin size decreased the correlation between the 2D and 3D images thereby decreasing the robustness of the algorithm, while decreasing the bin size caused false positives in transformation matches. There is also the opportunity to investigate selective point sampling to provide sufficient information in characterizing the image without compromising information retained.

6.2.5 Optimization Method

The covariance function is very sensitive to the topology of the shape distribution. The sample statistic cross-correlation coefficient r is not robust, so its value can be misleading if outliers are present [37]. It may not be the best optimization method for this scenario. Other methods should be explored to match the needs of the data type and output. Additionally, strategic evaluation criteria will address the degeneracy of the solution set.

6.2.6 Precision

This algorithm indicates the potential for nearly infinite precision and accuracy of patient positioning. The shape distribution currently holds to sub-pixel accuracy, as based on pixel interval base transformations. The fourth set of experimental results shows the potential for further precision and accuracy by improving the optimization algorithm for analysis of interpolation and extrapolation of the linear relationships developed between the correlation matrices.

6.3 Concluding Remarks

In the initial era of patient positioning for radiation treatment planning, attempts to verify beam alignment with target volume were limited by the poor quality and the cumbersome use of radiographic films [19]. Currently, patient positioning is a challenge during radiation therapy treatment as it is a process that takes a significant amount of time.

The shape distribution 2D-3D image registration method establishes a novel way to compute efficiently and accurately the relative 6-DoF transformation that maps the pair of 2D orthogonal images to the 3D volume base set. This technique avoids many of the issues related to current image registration methods. The method has the potential for application for other image modalities in image-guided patient positioning. With future research, the shape distribution method can become even more efficient and robust, and provide near infinite precision. We have achieved the main objective to introduce an accurate, fast, and robust patient-positioning algorithm to align the pre-operative information of the examined patient with rapid pose information of patient in the radiation treatment room.

Appendix A

Implementation Details

A.1 Base Transformation Set

```
INIT 2D-CT data
INIT N maximum perturbation for base transformation set
INIT Transformation set of T{N}

FUNCTION base
      CALL Generate DRR [17]
      GENERATE 3d volume from CT data
      FOR each transformation in transformation set
            CALL Transform
            GENERATE transformations of 3d volume
      ENDFOR
      FOR each transformed volume
            CREATE bi-planar projections of 3D volume
            FOR each projection
            CALL DataPreprocess
            CALL ShapeFunction
            CREATE shape distributions for each projection
            ENDFOR
      ENDFOR
ENDFUNCTION
```

A.2 Image Data Preprocessing

```
INIT anatomical range
FUNCTION DataPreprocess
      CROP image to anatomical range
      CALL FilterImage
ENDFUNCTION
```

A.3 Transformation

```
FUNCTION Transform
      CREATE translation and rotation transformation matrix
      TRANSFORM image by transformation matrix
ENDFUNCTION
```

A.4 Shape Function

```
INIT Isocenter
INIT Bone intensity range
INIT Bin size
FUNCTION ShapeFunction
      FOR every pixel in image
            COMPUTE Pixel intensity
            COMPUTE Distance from pixel to isocenter
            IF Pixel intensity is within bone intensity range
                  INCREASE Count at distance and intensity
            ENDIF
      ENDFOR
      CREATE Shape distribution from count histogram as number of points with
distance and intensity
      NORMALIZE Shape distribution
ENDFUNCTION
```

A.5 Objective Function

```
INIT P-value threshold
INIT Correlation coefficient threshold
FUNCTION Objective
      LOAD Base transformation set
      LOAD Input images
      CALL ShapeFunction on bi-planar input images
      CREATE Cross-correlation matrix between shape distribution of each input
image with those of the base projections
      CREATE P-value matrix
      GET Transformations of p-value transformations less than threshold and
      correlation higher than correlation coefficient threshold
ENDFUNCTION
```

A.6 Optimization

```
INIT transformation criteria
INIT rotation criteria
FUNCTION Optimization
      CALL Objective
      FOR each projection
            LOAD Correlation matrix
            GET Gradient of correlation matrix
            IDENTIFY potential translation transformation matches
            IDENTIFY potential rotation transformation matches
      ENDFOR
      FOR each degree-of-freedom
            DETERMINE transformation that optimizes objective function
      ENDFOR
ENDFUNCTION
```

Appendix B

Base Volume Set

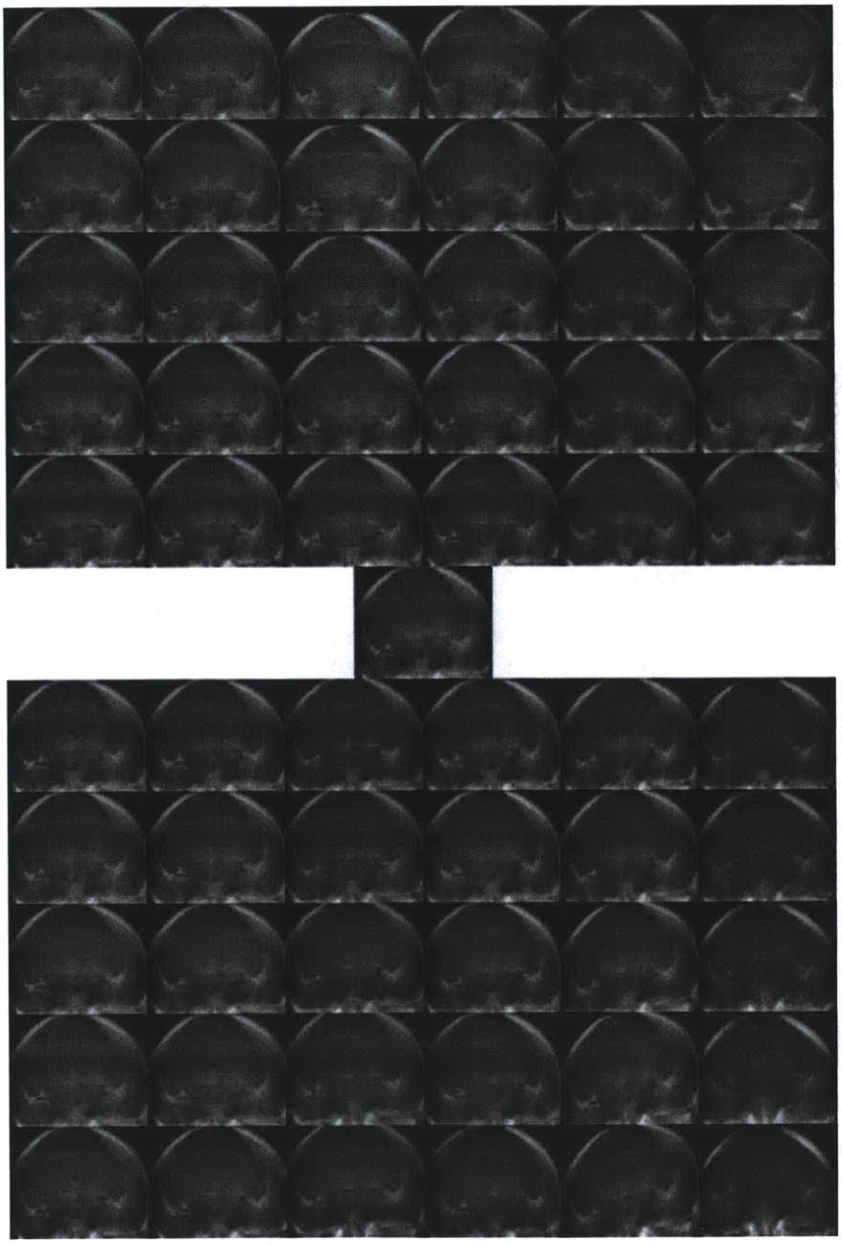

Figure B-1: Transformations *T* imposed on *V*, coronal projection. Layout conforms to *T* established in Table 4-1.

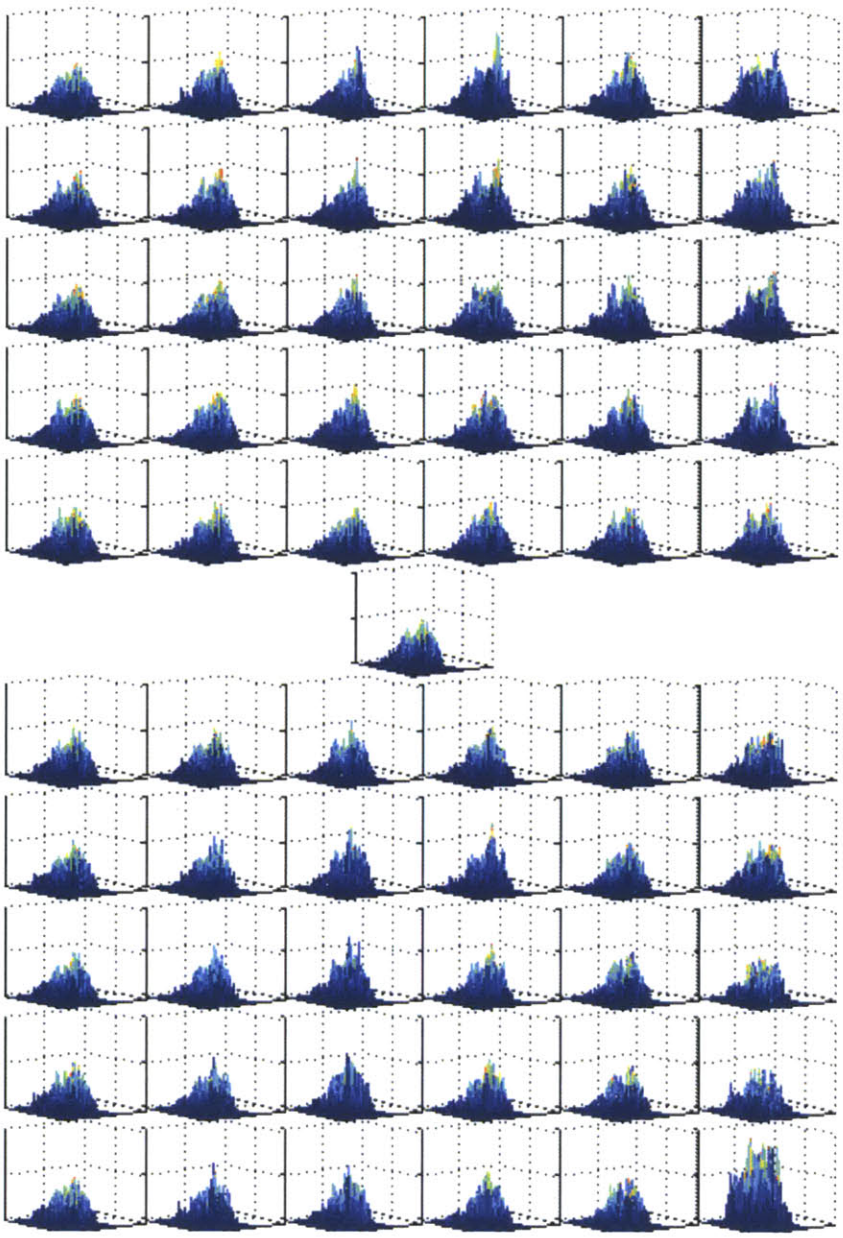

Figure B-2: Shape distributions SV_c evaluated as $F(V_c)$, coronal projection. Layout conforms to T established in Table 4-1.

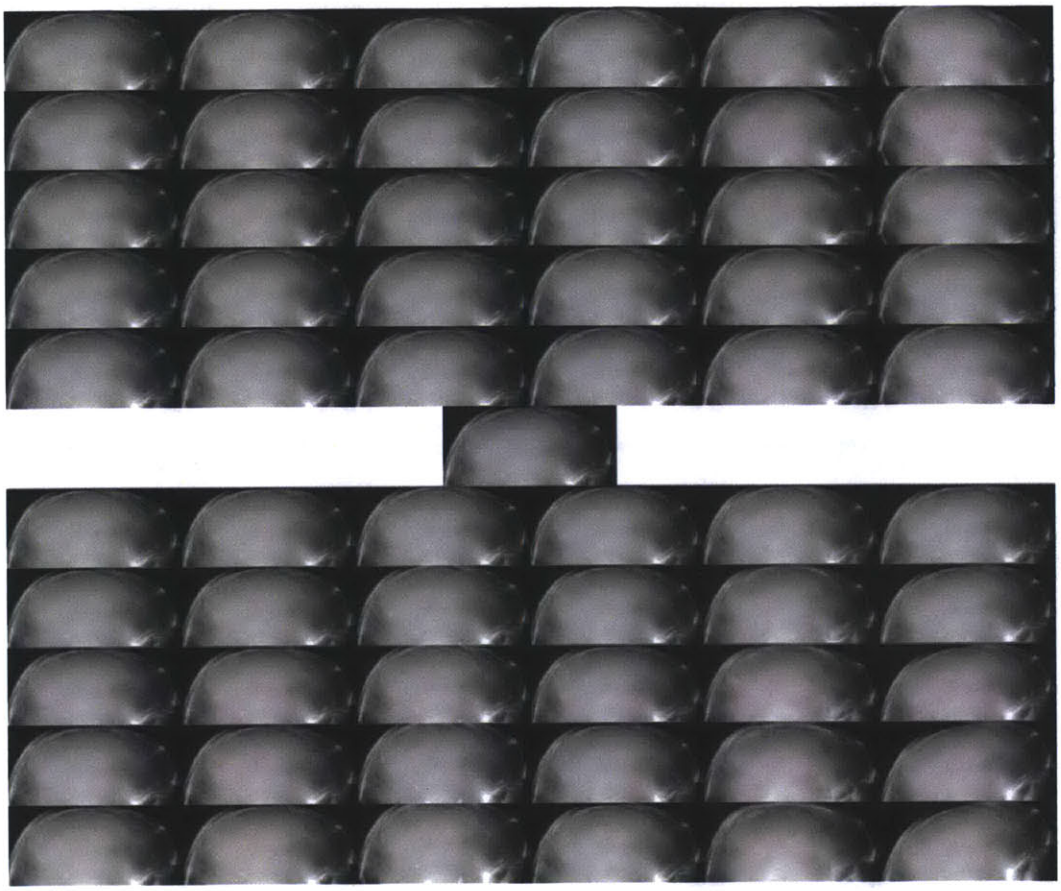

Figure B-3: Transformations *T* imposed on *V*, sagittal projection. Layout conforms to *T* established in Table 4-1.

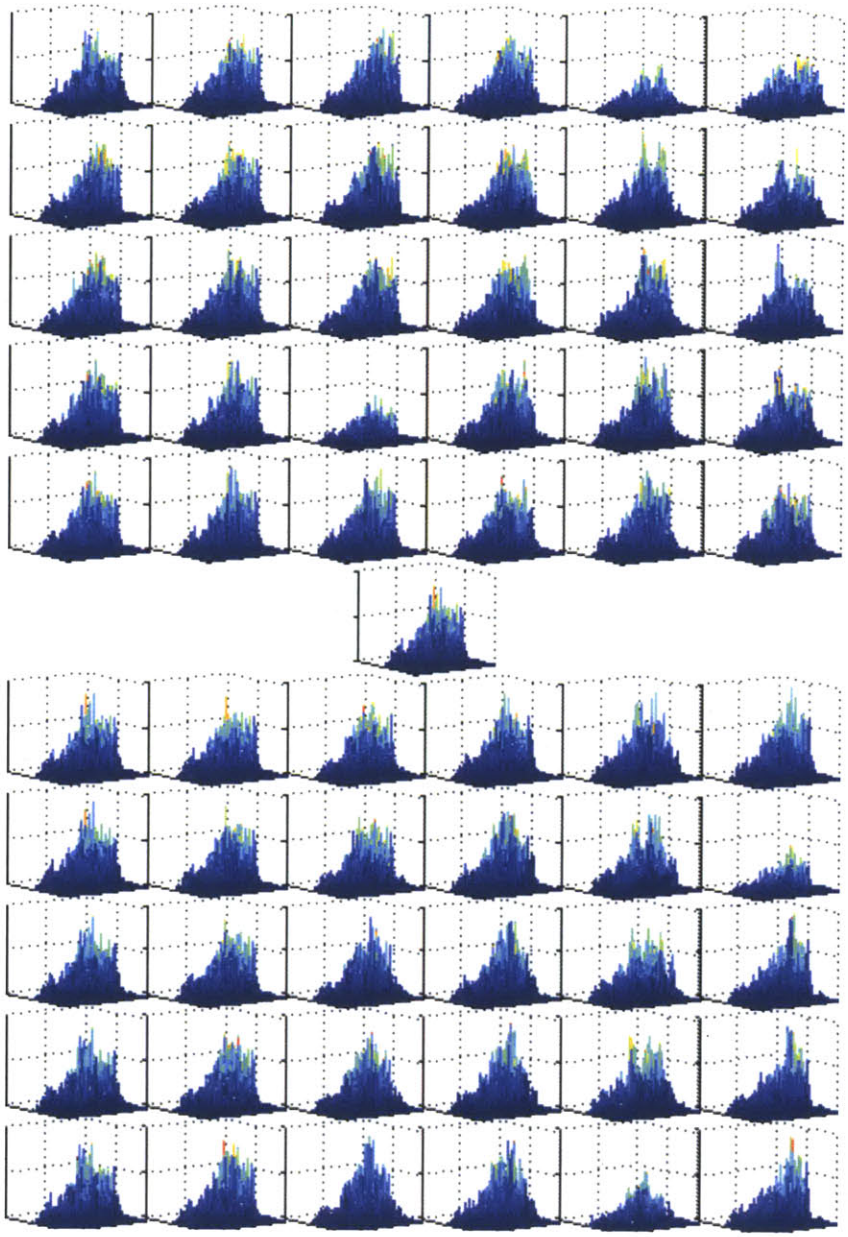

Figure B-4: Shape distributions SV_s evaluated as $F(V_s)$, sagittal projection. Layout conforms to T established in Table 4-1.

Appendix C

Shape Distributions

Additional shape functions proposed by Osada *et al.* are shared below [30].

A3: Measures the angle between three random points on the surface of a 3D model.
D1: Measures the distance between a fixed point and one random point on the surface. The centroid of the boundary of the model is treated as the fixed point.
D2: Measures the distance between two random points on the surface.
D3: Measures the square root of the area of the triangle between three random points on the surface.
D4: Measures the cube root of the volume of the tetrahedron between four random points on the surface.

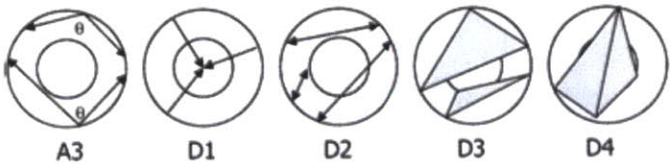

Figure C-1: Five simple shape functions based on angles (A3), lengths (D1 and D2), areas (D3), and volumes (D4).

Some of these shape functions may be adapted for use in extending the shaped distribution based image registration algorithm.

Appendix D

Small Angle Rotation

We approximate the transformation T as small-scale perturbations. In the following calculations, we prove the parameterization of rotation transformations with the equivalent angle-axis notation.

The rotation operator is represented as a 3D vector r where the length of the vector equals the rotation angle θ, $n\hat{}$ is a unit length vector, and the direction represents the rotation axis.

$$\theta = sqrt(r_x^2 + r_y^2 + r_z^2)$$

Thus, with the application of Rodrigue's formula, the rotation of a given 3D coordinate point is:

$$R(r,x) = x * \cos(\theta) + \hat{n}(\hat{n} \cdot x)(1 - \cos\theta) + \sin\theta(\hat{n} \times x)$$

And for small angles $\theta << 1$, the rotation can be approximated as:

$$R(r,x) \approx x + \theta(\hat{n} \times x) = x + r \times x$$

References

[1] "Cancer," World Health Organization: available on the Internet at < http://www.who.int/mediacentre/factsheets/fs297/en/> (February 2012).

[2] "Cancer Trends Progress Report," National Cancer Institute: available on the Internet at <http://progressreport.cancer.gov/doc_detail.asp?pid=1&did=2009&chid=93&coid=920&mid> (March 11, 2012).

[3] "World," Globocan 2008: available on the Internet at <http://globocan.iarc.fr/factsheets/populations/factsheet.asp?uno=900> (Jan 3, 2012).

[4] "Types of Treatment," National Cancer Institute at the National Institute of Health: available on the Internet at <http://www.cancer.gov/cancertopics/treatment/types-of-treatment> (March 17, 2012).

[5] F. Khan, *The Physics of Radiation Therapy,* Lippincott Williams & Wilkins, p. 264 (2009).

[6] "Radiation Therapy for Cancer," National Cancer Institute at the National Institute of Health: available on the Internet at <http://www.cancer.gov/cancertopics/factsheet/Therapy/radiation> (March 22, 2012).

[7] "Fast facts about radiation therapy." American Society for Radiation Oncology (ASTRO): available on the Internet at <http://www.astro.org/PressRoom/FastFacts/documents/FFAboutRT.pdf> (November 2010.)

[8] Y. Lievens and W. Van den Bogaert, "Proton beam therapy: too expensive to become true?," Radiotherapy and oncology: journal of the European Society for Therapeutic Radiology and Oncology,75(2):131, (2005).

[9] J.E. Tepper. Protons and parachutes. *Journal of Clinical Oncology,* 26(15): 2436, (2008).

[10] R. Robison, "History of Radiation Therapy," RT Answers: available on the Internet at <http://www.rtanswers.org/aboutus/history.aspx> (March 31, 2010).

[11] E. Hall and A. Giaccia, *Radiobiology for the Radiologist,* Wolters Kluwer: Philadelphia, PA (2012).

[12] M. Kessler and K. Li, "Image Fusion for Conformal Radiation Therapy," AAPM Annual Meeting, Salt Lake City, Utah, July 22-26, 2001, American Association of Physicists in Medicine: available on the Internet at <http://www.aapm.net/meetings/2001AM/pdf/7213-95766.pdf> (2001).

[13] T. Bortfeld, R. Schmidt-Ullrich, W. De Neve, D. Wazer, *Image-Guided IMRT,* Springer. (2005).

[14] F. Sterzing, R. Engenhart-Cabilic, M. Rentje, J. Debus, "Options of Image-Guided Radiotherapy – a New Dimension in Radiation Oncology," Dtsch Artzebl International, 08(16): 274–80. (2011).

[15] A. Del Guerra, *Ionizing Radiation Detectors for Medical Imaging.* Ch. 1, p. 9, World Scientific Publishing Co, Singapore, (2004).

[16] C.T. Metz, *Digitally Reconstructed Radiographs.* Utrecht University (2005).

[17] M. Folkerts, "DRR" [Computer Program]: available on the Internet at < http://www.cart.ucsd.edu/people/students/michaelfolkerts> (Sept. 2009).
[18] J. Flanz, "What's new in particle therapy accelerator technology," Massachusetts General Hospital: available on the Internet at <http://dx.doi.org/10.1016/j.nimb.2007.04.247> (2007).
[19] D. Verellen, M. De Ridder, N. Linthout, K. Tournel, G. Soete, G. Storme, "Innovations in Image-guided Radiotherapy," *Nature*, **24**, p. 949-960 (2007).
[20] N. Morrow, C. Stepaniak, J. White, J. Wilson, and X. Li, "Inter-fractional setup uncertainty and intra- fractional motion for prone breast irradiation," Medical College of Wisconsin, (October 13, 2006).
[21] B. Fraass, et al, "Integration of magnetic resonance imaging into radiation therapy treatment planning: I. Technical considerations," *Int J Radiat Oncol Biol Phys*, 13:1897-908, (1987).
[22] Schad LR, Loot S, Schmidt F, Sturm V, Lorenz WJ, "Correction of spatial distortion in MR imaging: a prerequisite for accurate stereotaxy," J *Comput Assist Tomogr*, 11:499-505. (1987).
[23] "Applications of Nuclear Techniques in Medicine," International Atomic Energy Agency: available on the Internet at <http://www.iaea.org/Publications/Factsheets/English/ntimedic.html> (August 8, 2011).
[24] B. Zitová and J. Flusser, "Image registration methods: a survey," Image Vision and Computing, 21, p. 997-1000, (2003).
[25] A. Goshtabsby, "Image Registration: Introduction," Wright State University and Image Fusion Systems Research: available on the Internet at <http://www.imgfsr.com/IntroductionCVPR.pdf> (June 27, 2004).
[26] P. Markelj, D. Tomaževič, B. Likar, and F. Pernuš, "A review of 3D/2D registration methods for image-guided interventions," Medical Image Analysis. doi:10.1016/j.media.2010.03.005 (2010).
[27] A. Gruen, D. Akca, "Least Squares 3D Surface and Curve Matching." *ISPRS Journal of Photogrammetry & Remote Sensing*, 59, 151-174, (2005).
[28] D. Dementhon, P. David, H. Samet. (2001) "SoftPOSIT: An Algorithm for Registration of 3D Models to Noise Perspective Images Combining SoftAssign and POSIT." Center for Automation Research. 1-27.
[29] W. Crum, T. Hartkens, D. Hill. (2004) "Non-rigid image registration: theory and practice." The British Journal of Radiology, 77, 140-153.
[30] R. Osada, T. Funkhouser, B. Chazelle, D. Dobkin, "Shape Distributions," *ACM Transaction on Graphics*, 21, 807-832 (2002).
[31] S. Meroli, "Noise Analysis of Particle Sensors and Pixel Detectors," available on the Internet at http://meroli.web.cern.ch/meroli/Lecture_Particle_Detector_Noise.html> (2010).
[32] T. Rowland and E. Weisstein, "Linear Transformation," Mathworld – A Wolfram Web Resource: available on the Internet at <http://mathworld.wolfram.com/LinearTransformation.html> (July 8, 2011).
[33] P. Bourke. "AutoCorrelation – 2D Pattern Identification," available on the Internet at <http://paulbourke.net/miscellaneous/correlate/> (August 1996).
[34] I. T. Jolliffe, "Principle Component Analysis." Springer (2002).

[35] D. Fu and G. Kuduvalli, "A fast, accurate, and automatic 2D–3D image registration for image-guided cranial radiosurgery," *Medical Physics*, 35, 5, p. 2180-2194 (2008).
[36] "Optimizing for Speed," available on the Internet at < http://www.caspur.it/risorse/softappl/doc/matlab_help/techdoc/matlab_prog/ch8_pr18.html> (February 25, 2012.)
[37] R. Wilcox, Introduction to robust estimation and hypothesis testing. Academic Press. (2005).
[38] L. Zöllei, "2D-3D Rigid-Body Registration of X-ray Fluoroscopy and CT Images," MS Thesis, Massachusetts Institute of Technology, Department of Electrical Engineering and Computer Science (August 2001).